Cell Stem Cell

Article

m^{6}A deficiency impairs hypothalamic neurogenesis of feeding-related neurons in mice and human organoids and leads to adult obesity in mice

Graphical abstract

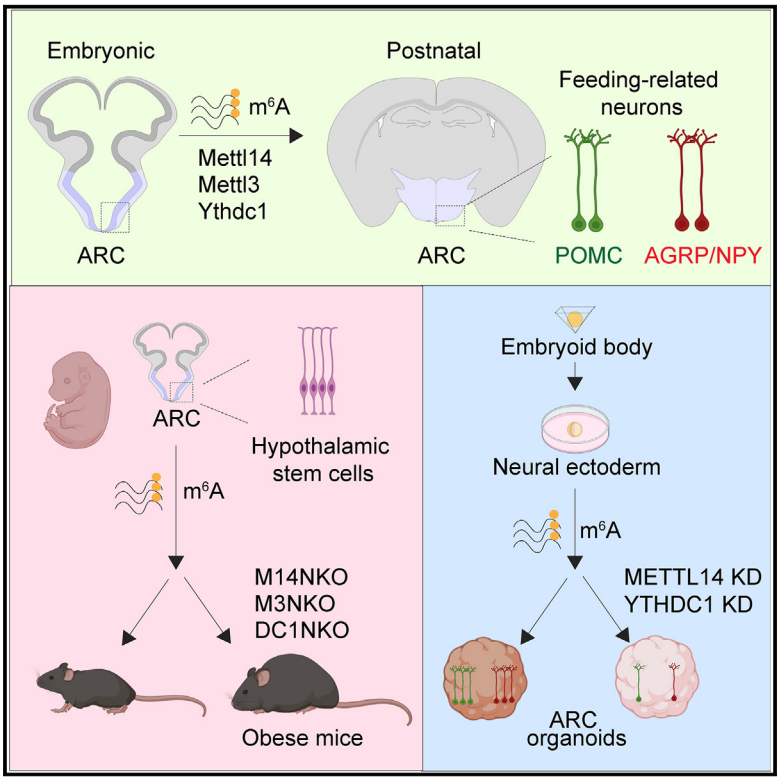

Authors

Yachen Shen,
Samuel Zheng Hao Wong, Tong Ma, ...,
Chuan He, Guo-li Ming, Hongjun Song

Correspondence

gming@pennmedicine.upenn.edu (G.-l.M.),
shongjun@pennmedicine.upenn.edu (H.S.)

In brief

Shen et al. revealed a conserved role of Mettl14/Ythdc1-dependent m^{6}A signaling in arcuate nucleus neurogenesis of feeding-related neurons in mice and human organoids. Furthermore, deletion of Mettl14 in mice leads to adult obesity. These results shed light on the developmental basis of epitranscriptomic regulation of food intake and energy homeostasis.

Highlights

- Embryonic hypothalamic *Mettl14* deletion results in adult obesity in mice
- *Mettl14*, Mettl3, or Ythdc1 cKO mice exhibit arcuate nucleus neurogenesis deficits
- Arcuate nucleus-specific organoids derived from feeder-free human iPSCs
- *METTL14* or *YTHDC1* knockdown reduces feeding-related neurons in human organoids

Shen et al., 2025, Cell Stem Cell *32*, 727–743
May 1, 2025
https://doi.org/10.1016/j.stem.2025.02.011

CellPress

Cell Stem Cell

CellPress

Article

m^{6}A deficiency impairs hypothalamic neurogenesis of feeding-related neurons in mice and human organoids and leads to adult obesity in mice

Yachen Shen,[1,2] Samuel Zheng Hao Wong,[1] Tong Ma,[1] Feng Zhang,[1] Qing Wang,[8] Riki Kawaguchi,[8] Daniel H. Geschwind,[8] Jeremy Wang,[9] Chuan He,[10,11] Guo-li Ming,[1,3,4,5,*] and Hongjun Song[1,3,5,6,7,12,*]

[1]Department of Neuroscience and Mahoney Institute for Neurosciences, Perelman School of Medicine, University of Pennsylvania, Philadelphia, PA, USA
[2]Department of Pathology and Laboratory Medicine, Perelman School of Medicine, University of Pennsylvania, Philadelphia, PA, USA
[3]Department of Cell and Developmental Biology, Perelman School of Medicine, University of Pennsylvania, Philadelphia, PA, USA
[4]Department of Psychiatry, Perelman School of Medicine, University of Pennsylvania, Philadelphia, PA, USA
[5]Institute for Regenerative Medicine, Perelman School of Medicine, University of Pennsylvania, Philadelphia, PA, USA
[6]Epigenetics Institute, Perelman School of Medicine, University of Pennsylvania, Philadelphia, PA, USA
[7]Department of Neurosurgery, Perelman School of Medicine, University of Pennsylvania, Philadelphia, PA, USA
[8]Program in Neurogenetics, Department of Neurology, David Geffen School of Medicine, University of California, Los Angeles, Los Angeles, CA, USA
[9]Department of Biomedical Sciences, University of Pennsylvania School of Veterinary Medicine, Philadelphia, PA, USA
[10]Department of Chemistry, Howard Hughes Medical Institute, the University of Chicago, Chicago, IL, USA
[11]Department of Biochemistry and Molecular Biology, Howard Hughes Medical Institute, the University of Chicago, Chicago, IL, USA
[12]Lead contact
*Correspondence: gming@pennmedicine.upenn.edu (G.-l.M.), shongjun@pennmedicine.upenn.edu (H.S.)
https://doi.org/10.1016/j.stem.2025.02.011

SUMMARY

N^6-methyladenosine (m^{6}A), the most prevalent internal modification on mRNAs, plays important roles in the nervous system. Whether neurogenesis in the hypothalamus, a region critical for controlling appetite, is regulated by m^{6}A signaling, especially in humans, remains unclear. Here, we showed that deletion of m^{6}A writer Mettl14 in the mouse embryonic hypothalamus led to adult obesity, with impaired glucose-insulin homeostasis and increased energy intake. Mechanistically, deletion of Mettl14 leads to hypothalamic arcuate nucleus neurogenesis deficits with reduced generation of feeding-related neurons and dysregulation of neurogenesis-related m^{6}A-tagged transcripts. Deletion of m^{6}A writer Mettl3 or m^{6}A reader Ythdc1 shared similar phenotypes. METTL14 or YTHDC1 knockdown also led to reduced generation of feeding-related neurons in human brain subregion-specific arcuate nucleus organoids. Our studies reveal a conserved role of m^{6}A signaling in arcuate nucleus neurogenesis in mice and human organoids and shed light on the developmental basis of epitranscriptomic regulation of food intake and energy homeostasis.

INTRODUCTION

Accumulative studies have revealed important roles for a variety of dynamic RNA modifications in many biological processes, including N^6-methyladenosine (m^{6}A), N^1-methyladenosine (m^{1}A), 5-methylcytosine (m^{5}C), and pseudouridine (ψ).[1,2] Among these RNA modifications, m^{6}A is the most prevalent internal modification of mRNA in eukaryotic cells.[3,4] The deposition of m^{6}A is orchestrated by m^{6}A methyltransferases, referred to as "writers," which include the METTL3/METTL14 complex and METTL16.[5–11] m^{6}A can be enzymatically removed by m^{6}A demethylases, known as "erasers," including fat mass and obesity-associated (FTO) and AlkB homolog 5 (ALKBH5).[12,13] Functionally, m^{6}A modifications can be recognized by various m^{6}A-binding proteins, known as "readers," such as YTH N^6-methyladenosine RNA-binding proteins (YTHDFs) and YTH domain-containing families (YTHDCs), to regulate RNA metabolism.[14] m^{6}A is prominently enriched in the mammalian nervous system and plays important roles in diverse biological processes, including cortical neurogenesis, cerebellar development, adult neurogenesis, memory formation and consolidation, and axonal regeneration.[15–22] In particular, m^{6}A signaling regulates the tempo but not the neuronal fate specification of neural stem cells during embryonic cortical neurogenesis.[20] Whether m^{6}A signaling plays a similar or distinct role in neurogenesis in different brain regions is not well understood.

The hypothalamus, an evolutionarily conserved region in the brain, serves as a central regulator of energy intake, expenditure, and fat storage.[23,24] Within the hypothalamus, numerous nuclei comprised of distinct sets of neurons orchestrate a wide array of functions.[25,26] One of these nuclei, known as the arcuate

nucleus (ARC), has been characterized as a pivotal hub for regulating feeding behavior,[27] where anorexigenic proopiomelanocortin (POMC)-expressing neurons and orexigenic neuropeptide-Y (NPY)/agouti-related peptide (AgRP)-expressing neurons play important but contrasting roles.[28–30] The proper function of the hypothalamus relies on a meticulously orchestrated developmental process.[25,31–34] Deficits in hypothalamus development have been linked to various disorders, including obesity and diabetes.[35] In both mouse and human brains, the hypothalamus is one of the brain regions with the most abundant levels of m^{6}A.[36] Whether m^{6}A also plays a regulatory role in hypothalamic neurogenesis and functions, especially in humans, remains unknown.

Several studies indicate that dysfunctional m^{6}A modifications may contribute to various metabolic diseases, including obesity, type 2 diabetes, and metabolic syndrome.[37,38] Genome-wide association studies (GWASs) in humans have identified intronic single nucleotide polymorphisms (SNPs) within the locus of *FTO* to be strongly correlated with the body mass index of individuals with obesity.[39,40] However, later studies suggest that these SNPs do not affect *FTO* expression but instead may regulate the expression of two nearby genes *IRX3* and *RPGRIP1L*.[41–43] On the other hand, global overexpression of *FTO* in mice led to elevated body and fat mass and food intake,[44] however, the underlying mechanism is not well understood. While FTO can function as an m^{6}A demethylase, it can also demethylate N6,2′-O-dimethyladenosine (m^{6}A$_m$) in the 5′ cap of mRNA to promote mRNA stability with even higher *in vitro* enzymatic activity compared with m^{6}A as a substrate.[45] Therefore, whether m^{6}A signaling is directly involved in regulating fat and body mass and food intake remains unclear. Given the contrasting evidence from human genetics and mouse studies, whether m^{6}A signaling, particularly in the hypothalamus, plays a similar or different role related to obesity in mice and in humans is an important question that requires appropriate human cell-based models to address. Brain region-specific organoids derived from human induced pluripotent stem cells (iPSCs) have emerged as exciting experimental models to investigate human brain development and disorders[46–49] and provide an opportunity to explore this question.

Here, we investigated the role of m^{6}A writers and readers in regulating hypothalamic neurogenesis using multiple genetic mouse models *in vivo* and an improved human iPSC-derived brain subregion-specific ARC organoid (ARCO) model *in vitro*. Our study illuminates the pivotal and conserved role of m^{6}A signaling in the generation of feeding-related hypothalamic neurons in both mice and human organoids and highlights that disruptions in m^{6}A signaling pathways in the developing mammalian hypothalamus are linked to adult obesity.

RESULTS

Embryonic hypothalamic *Mettl14* deletion leads to obesity in adult mice

To explore the functional role of m^{6}A in the developing hypothalamus, we conditionally deleted the m^{6}A writer Mettl14 in the embryonic basal hypothalamic region by crossing Nkx2.1-Cre mice[50–52] with Mettl14$^{f/f}$ mice[20] to generate Nkx2.1-Cre::Mettl14$^{f/f}$ mice (named M14NKO thereafter). Both male and female M14NKO mice exhibited an accelerated rate of weight gain compared with their Mettl14$^{f/f}$ control (CTRL) littermates after early postnatal stages, resulting in pronounced obesity in adult mice, whereas the Nkx2.1-Cre::Mettl14$^{f/+}$ mice did not exhibit any differences in body weight compared with CTRL mice (Figures 1A, S1A, and S1B). Analysis of the body composition through magnetic resonance imaging (MRI) at 16 weeks revealed that the weight gain in M14NKO mice was predominantly attributed to an increase in fat mass, which was five times greater than in CTRL mice, whereas the lean mass was similar in female mice but modestly reduced in male mice (Figure 1B). The inguinal white adipose tissue (iWAT), female gonadal white adipose tissue (gWAT), male epididymal white adipose tissue (eWAT), and brown adipose tissue (BAT) exhibited larger volumes, and their adipocytes showed greater hypertrophy in M14NKO mice compared with those in CTRL mice (Figures 1C and 1D). To further characterize the obesity-related diabetic phenotypes, we examined glucose homeostasis. Glucose tolerance tests (GTTs) and insulin tolerance tests (ITTs) showed hyperglycemia and insulin resistance in M14NKO mice, compared with their CTRL littermates, for both sexes (Figures 1E–1H). Additionally, upon overnight fasting, the glucose and insulin levels were elevated in M14NKO mice for both sexes, indicating a diminished effect from circulating insulin (Figures S1C and S1D). Thus, a loss of Mettl14 in the developing hypothalamus leads to an augmentation in fat mass, adult obesity, and dysregulated glucose homeostasis.

To dissect potential factors contributing to obesity, we conducted experiments with mice housed in metabolic cages. Both adult male and female M14NKO mice exhibited increased food intake compared with CTRL mice (Figure 2A). There was a positive correlation of energy expenditure with body weight in both M14NKO mice and their CTRL littermates (Figure 2B) and a decrease in the energy expenditure of M14NKO mice when normalized to body weight (Figure 2C). There was also a decrease in oxygen consumption (VO_2) and carbon dioxide production (VCO_2) in M14NKO mice for both sexes when normalized to body weight (Figures 2D–2G). Female M14NKO mice exhibited a modest reduction in the respiratory exchange ratio (RER), whereas no changes were observed in male M14NKO mice (Figures 2H and 2I). Furthermore, adult M14NKO mice exhibited dramatically reduced locomotor activity compared with CTRL mice for both sexes (Figures 2H and 2I).

Embryonic hypothalamic *Mettl14* deletion leads to decreased numbers of feeding-related neurons in the ARC

To explore the cellular mechanism underlying *Mettl14*-deletion-induced obesity, we examined the neuronal composition of ARC, which is composed of multiple neuronal subtypes that play crucial roles in regulating feeding behavior and energy balance.[27] For a systematic analysis, we performed single-cell RNA sequencing (scRNA-seq) on the micro-dissociated ARC region from individual M14NKO mice and their CTRL littermates (four pairs) at postnatal day 0 (P0) (Figure S2A). Based upon the expression levels of marker genes for each cell type,[26,33,53,54] we classified a total of 19,020 cells (wild type [WT]: 9,111; M14NKO: 9,909) into 10 distinct clusters, including neurons (*Tubb3*$^+$, *Syt1*$^+$), ependymocytes (*Foxj1*$^+$), tanycytes (*Col23a1*$^+$), oligodendrocyte cells (*Pdgfra*$^+$), oligodendrocyte precursor cells (OPCs) (*Top2a*$^+$), peripheral vascular macrophage and microglia (PVMMicro) (*Cx3cr1*$^+$), endothelial cells (*Foxj1*$^+$), intermediate progenitor cells (IPCs) (*Ascl1*$^+$),

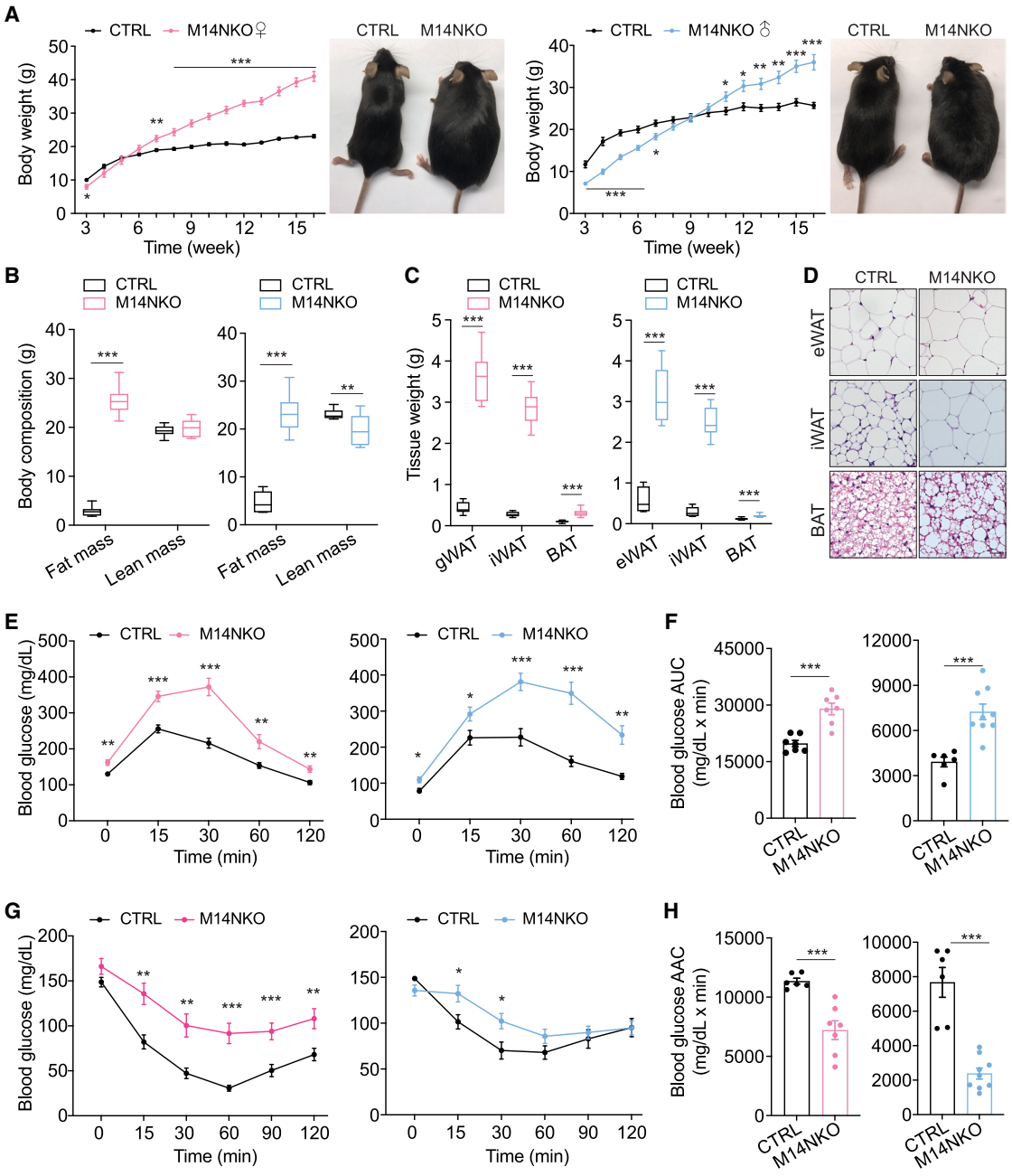

Figure 1. Embryonic hypothalamic *Mettl14* deletion leads to adult obesity and dysfunction of systemic glucose homeostasis in mice

(A) Body weight of CTRL (Mettl14$^{f/f}$) and M14NKO (Nkx2.1-Cre:Mettl14$^{f/f}$) female (left) and male (right) mice. Values represent mean ± SEM (female: n = 8/CTRL and 8/M14NKO; male: n = 6/CTRL and 9/M14NKO; *p < 0.05, **p < 0.01, ***p < 0.001, Student t test).

(B and C) Boxplot of body mass (B) and adipose depot weight (C) of 16-week-old female and male CTRL and M14NKO mice. Same sets of animals as in (A). For box plots, the central line is the median, and the interquartile range is shown (**p < 0.01, ***p < 0.001, Student t test). gWAT, gonadal white adipose tissue; eWAT, epididymal white adipose tissue; iWAT, inguinal white adipose tissue; BAT, brown adipose tissue.

(D) H&E staining of gWAT, iWAT, and BAT of 16-week-old female CTRL and M14NKO mice. Scale bar, 25 μm. Note the adipocyte hypertrophy in M14NKO mice.

(E and F) Glucose tolerance test (E) and area under curve (AUC) (F) in 10-week-old female CTRL and M14NKO mice (left) and in 12-week-old male CTRL and M14NKO mice (right). Same sets of animals as in (A). Values represent mean ± SEM (*p < 0.05, **p < 0.01, ***p < 0.001, Student t test).

(G and H) Insulin tolerance test (G) and area above curve (AAC) (H) in 11-week-old female CTRL and M14NKO mice (left) and in 13-week-old male CTRL and M14NKO mice (right). Same sets of animals as in (A). Values represent mean ± SEM (*p < 0.05, **p < 0.01, ***p < 0.001, Student t test).

See also Figure S1 and Table S2.

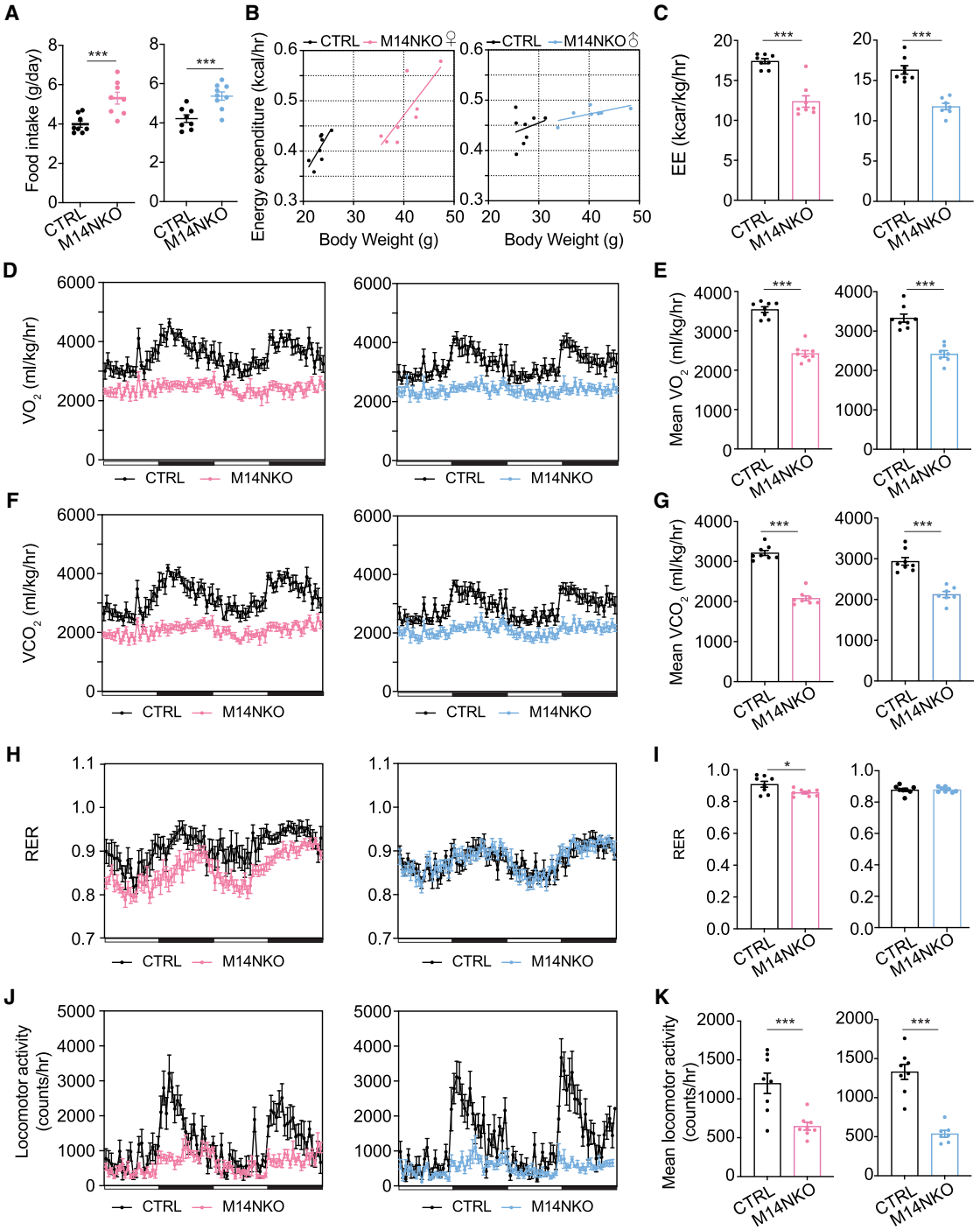

Figure 2. Embryonic hypothalamic *Mettl14* ablation results in impaired energy balance in adult mice

(A) Food intake in 13-week-old female CTRL and M14NKO mice and 14-week-old male CTRL and M14NKO mice. Same set of animals as in Figure 1A. Values represent mean ± SEM (*$p < 0.05$, **$p < 0.01$, ***$p < 0.001$, Student t test).

(B and C) Regression plots of mean hourly energy expenditure (y axis) correlated to body weight (x axis) in female (left) and male (right) CTRL and M14NKO mice for 48 h (B) and mean hourly energy expenditure normalized by body weight (C). Same sets of animals as in (A). In (C), values represent mean ± SEM (*$p < 0.05$, **$p < 0.01$, ***$p < 0.001$, Student t test).

(D and E) O_2 consumption normalized by body weight in female (left) and male (right) CTRL and M14NKO mice for 48 h (D) and mean O_2 consumption rate normalized by body weight (E). Open boxes: bright period of time (7:00–19:00); black boxes: dark period of time (19:00–7:00) (E). Same sets of animals as in (A). Values represent mean ± SEM (*$p < 0.05$, **$p < 0.01$, ***$p < 0.001$, Student t test).

(legend continued on next page)

astrocytes (*Aldh1l1*$^+$), and vascular and leptomeningeal cells (VLMCs) (*Col3a1*$^+$) (Figures S2B and S2C). Among non-neuronal clusters, we noted a significant increase in the percentage of IPCs and tanycytes in M14NKO mice compared with CTRL mice (Figure S2D). We also detected differential gene expression in some non-neuronal cell types between M14NKO and CTRL mice (Table S1).

We then focused on the neuronal cluster of 10,415 neurons (WT: 5,119; M14NKO: 5,296) and subclustered them into 33 clusters, including 20 clusters from the ARC neurons based on published reference scRNA-seq datasets[26,33,53,54] (Figures 3A and 3B). We did not find any distinct neuronal clusters exclusive to M14NKO mice (Figure 3A). On the other hand, the composition ratios of neuronal clusters in the ARC and non-ARC regions were different between the M14NKO and CTRL mice, with an increased percentage of Ssr2/Tbx3 cluster neurons and decreased percentages of Pomc/Tbx3, Trh/Otp, Arx/Dlx1, Cbln2/Nts, Th/Dlx1, Agrp/Npy/Otp, and Avp/Sst cluster neurons among all neurons in M14NKO mice (Figures 3B and S2E). Both POMC$^+$ and AGRP$^+$ neurons are pivotal in regulating energy homeostasis.[28,55,56] Simultaneously, the expression levels of *Pomc*, *Agrp*, *Npy*, and *Otp* in related clusters were reduced in M14KO mice (Figure 3C). Across the transcriptome, we identified many differentially expressed genes in neurons within the Agrp/Npy/Otp cluster, Pomc/Tbx3 cluster, and Ssr2/Tbx3 cluster between M14NKO and CTRL mice (Figure S2F). Gene Ontology (GO) analysis revealed that downregulated genes in M14NKO mice are related to cell differentiation for the Agrp/Npy/Otp cluster, cholesterol biosynthetic process for the Pomc/Tbx3 cluster, and nervous system development for the Ssr2/Tbx3 cluster (Figure S2G). The transcription factor Otp is essential for the development of Agrp/Npy neurons[25,57,58] and was also observed to be expressed in Agrp/Npy neurons in previous studies[25,26] and in our scRNA-seq analysis (Figure 3C). To validate the finding of reduced numbers of feeding-related neurons in M14NKO mice, we performed immunohistological analysis of POMC$^+$ and OTP$^+$ neurons. Indeed, the numbers of POMC$^+$ and OTP$^+$ neurons were reduced in the ARC region in M14NKO mice compared with CTRL littermates both at P0 and in adult (Figures 3D and 3E). The reduction in POMC$^+$ neurons appeared more pronounced compared with OTP$^+$ neurons (Figures 3D and 3E). While the numbers of these specific neuronal subtypes were decreased, we found a slight increase in the total number of NeuN$^+$ neurons in the ARC region of M14NKO compared with CTRL mice (Figures 3F and 3G). These results suggest selective deficiencies in the number of particular neuronal subtypes, rather than a general reduction of all neurons in the ARC region with embryonic hypothalamic Mettl14 deletion.

Embryonic hypothalamic *Mettl14* deletion results in defective generation of POMC$^+$ neurons

To examine the generation of feeding-related neurons during embryonic hypothalamic neurogenesis directly, we performed a bromodeoxyuridine (BrdU) birth-dating experiment. In this assay, a pulse of BrdU incorporates into replicating DNA during the S-phase of the cell cycle and permanently marks the cell when it exits the cell cycle, whereas BrdU in progenitors after several rounds of cell division becomes diluted to undetectable levels by immunostaining[60,61] (Figure 4A). Pregnant mice were injected with a single dose of BrdU at either embryonic day (E)12.5 or E15.5, and the number of POMC$^+$BrdU$^+$ or NeuN$^+$BrdU$^+$ cells in the ARC region of CTRL or M14NKO mice was analyzed at P21 (Figure 4A). We observed a reduced number of NeuN$^+$BrdU$^+$ neurons in the ARC region of M14NKO mice compared with CTRL mice when BrdU was injected at E12.5, but an increased number when BrdU was injected at E15.5, indicating delayed neurogenesis in M14NKO mice (Figures 4B and 4C). Consistent with increased neurogenesis at E15.5, we found an increase in the number of Ki67$^+$ or PH3$^+$ cells in the ARC progenitor region of NKO compared with CTRL mice at E15.5 (Figures 4F and 4G). Importantly, there was a drastic reduction of POMC$^+$BrdU$^+$ neurons in the ARC region of the M14NKO mice compared with CTRL mice when BrdU was injected at E12.5 (Figures 4D and 4E). There was no further generation of POMC$^+$ neurons at E15.5 in either M14NKO or CTRL mice (Figures 4D and 4E). These results collectively support the model that Mettl14 deletion leads to delayed neurogenesis and a deficit in the generation of feeding-related neurons in the hypothalamus, which in turn leads to adult obesity.

Altered expression of some m^{6}A-tagged transcripts in hypothalamic neural progenitors

To further explore the mechanism underlying *Mettl14* regulation of hypothalamic neurogenesis, we knocked out *Mettl14* in neural progenitor cells (NPCs) derived from the embryonic hypothalamus of Mettl14$^{f/f}$ mice with lentivirus-mediated expression of Cre (Figure S3A). Consistent with *in vivo* findings, we observed reduced expression levels of Pomc and Agrp upon neuronal differentiation of Mettl14 KO hypothalamic NPCs *in vitro*, indicating deficits in neurogenesis of these feeding-related neuronal subtypes (Figure S3A). RNA-seq analysis identified 1,430 upregulated and 1,542 downregulated genes in Mettl14 KO hypothalamic NPCs compared with control hypothalamic NPCs without Cre expression (Figures S3B and S3C). GO analysis of downregulated genes revealed pathways related to nervous system development and cell differentiation (Figure S3D). In parallel, we performed m^{6}A sequencing to identify m^{6}A-tagged transcripts in control hypothalamic NPCs. We identified 21,020 m^{6}A peaks exhibiting a distinct RRACH (R = G/A, H = A/C/U) consensus motif and near the stop codon (Figures 5A and 5B). GO analyses revealed that m^{6}A-tagged transcripts were enriched in DNA repair, covalent chromatin modifications, histone modifications, cell cycle, regulation of mRNA metabolic process, and RNA splicing (Figure 5C). Next, we integrated differentially expressed transcripts from RNA-seq data with transcripts

(F and G) CO_2 production normalized by body weight in female (left) and male (right) CTRL and M14NKO mice for 48 h (F) and mean CO_2 consumption rate normalized by body weight (G). Same sets of animals as in (A). Values represent mean ± SEM (*$p < 0.05$, Student t test).
(H and I) Respiratory exchange ratio (RER) in female (left) and male (right) CTRL and M14NKO mice for 48 h (H) and mean RER (I). Same sets of animals as in (A). Values represent mean ± SEM (*$p < 0.05$, Student t test).
(J and K) Locomotor activity throughout 48 h in female (left) and male (right) CTRL and M14NKO mice (J) and mean locomotor activity (K). Same sets of animals as in (A). Values represent mean ± SEM (***$p < 0.001$, Student t test).

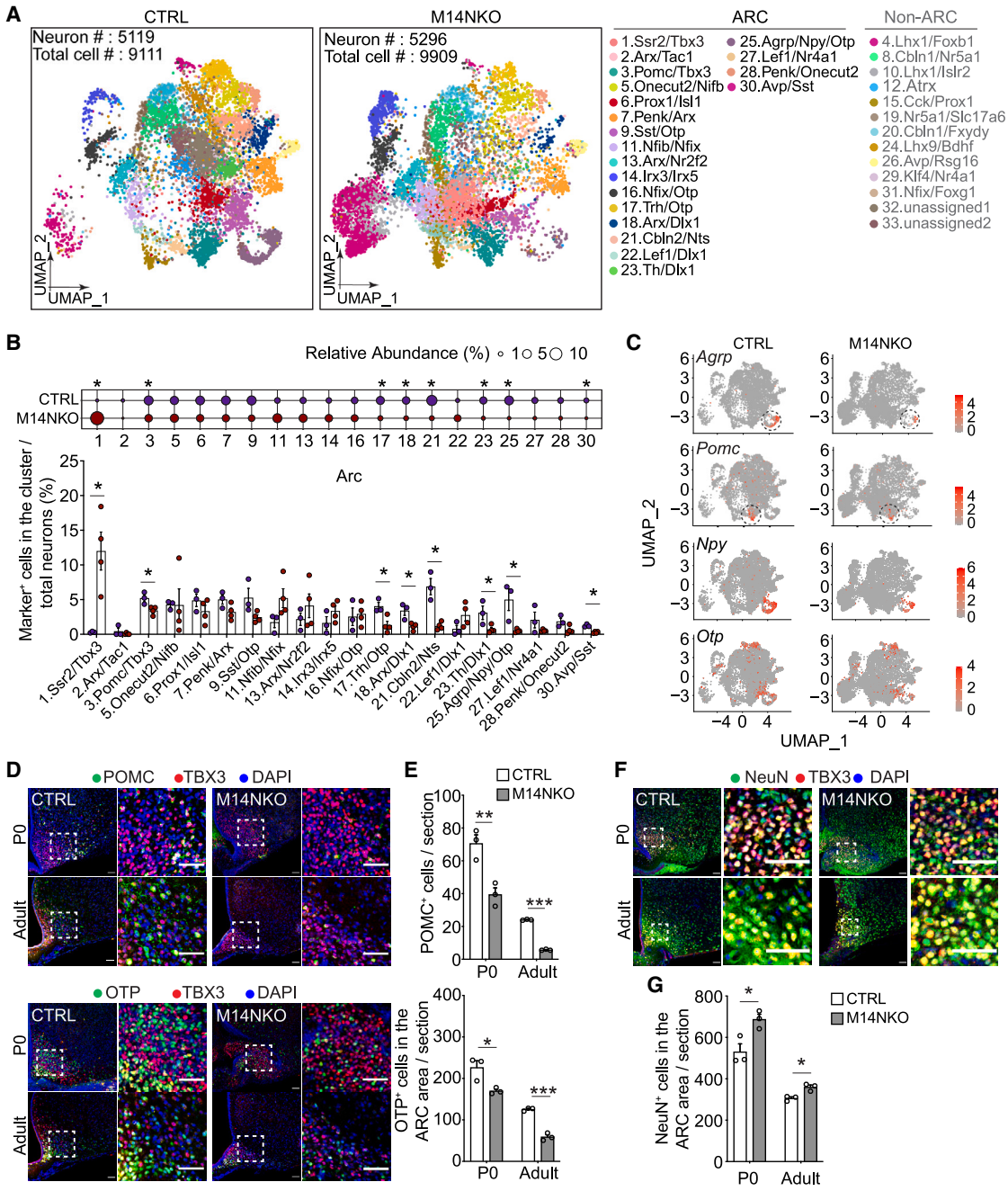

Figure 3. Embryonic hypothalamic *Mettl14* deletion leads to decreased numbers of feeding-related neurons in the arcuate nucleus of P0 and adult mice

(A) UMAP plot of neurons from 4 CTRL and 4 M14NKO mice, annotated according to known ARC and non-ARC neuron markers.[59]

(B) Quantification of the proportion of different ARC neuron clusters among the total number of neurons (A). Values represent mean ± SEM (n = 4/CTRL and 4/M14NKO; *p < 0.05; one-tailed Mann-Whitney test).

(C) Feature plots of *Pomc*, *Agrp*, *Npy*, and *Opt* expression levels in neurons from CTRL and M14NKO mice.

(D–G) Confocal sample images of POMC+, OTP+, and NeuN+ cells in the ARC of the hypothalamus from CTRL and M14NKO mice at P0 and adult (16 weeks) (D) and (F) and quantifications (E) and (G). Scale bars, 50 μm. Values represent mean ± SEM (n = 3 mice each; *p < 0.05, **p < 0.01, ***p < 0.001; Student's t test). See also Figure S2 and Table S1.

containing m^{6}A modifications in hypothalamic NPCs (Figures 5D and 5E). GO analysis of downregulated genes with m^{6}A modification revealed pathways related to nervous system development and cell differentiation (Figure 5F). The Wnt pathway is known for its crucial role in the development of the central nervous system.[62] We observed upregulation of genes associated

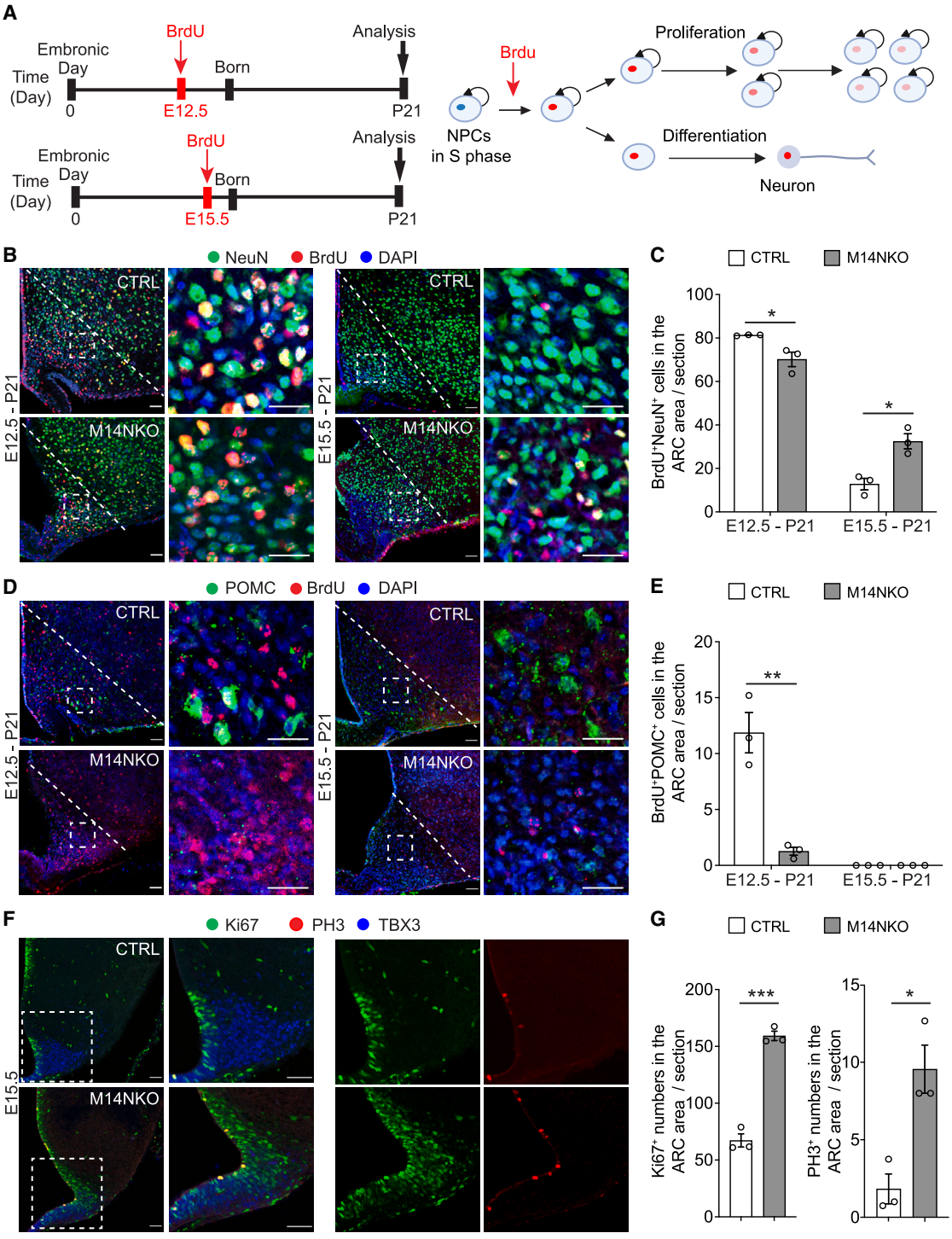

Figure 4. Embryonic hypothalamic *Mettl14* deletion impairs generation of POMC$^+$ neurons in mice

(A) A schematic diagram of experimental design of birth dating with BrdU.

(B–E) Confocal sample images of NeuN$^+$BrdU$^+$ and POMC$^+$BrdU$^+$ cells in the ARC region from P21 CTRL and M14NKO mice with BrdU injection at E12.5 (B) or E15.5 (D) and quantifications (C) and (E). Scale bars, 50 μm. Values represent mean ± SEM (n = 3 mice each; *p < 0.05, **p < 0.01, Student's t test).

(F and G) Confocal sample images of Ki67$^+$ and PH3$^+$ cells in the ARC region from CTRL and M14NKO mice at E15.5 (F) and quantifications (G). Scale bars, 50 μm. Values represent mean ± SEM (n = 3 mice each; *p < 0.05, ***p < 0.001, Student's t test).

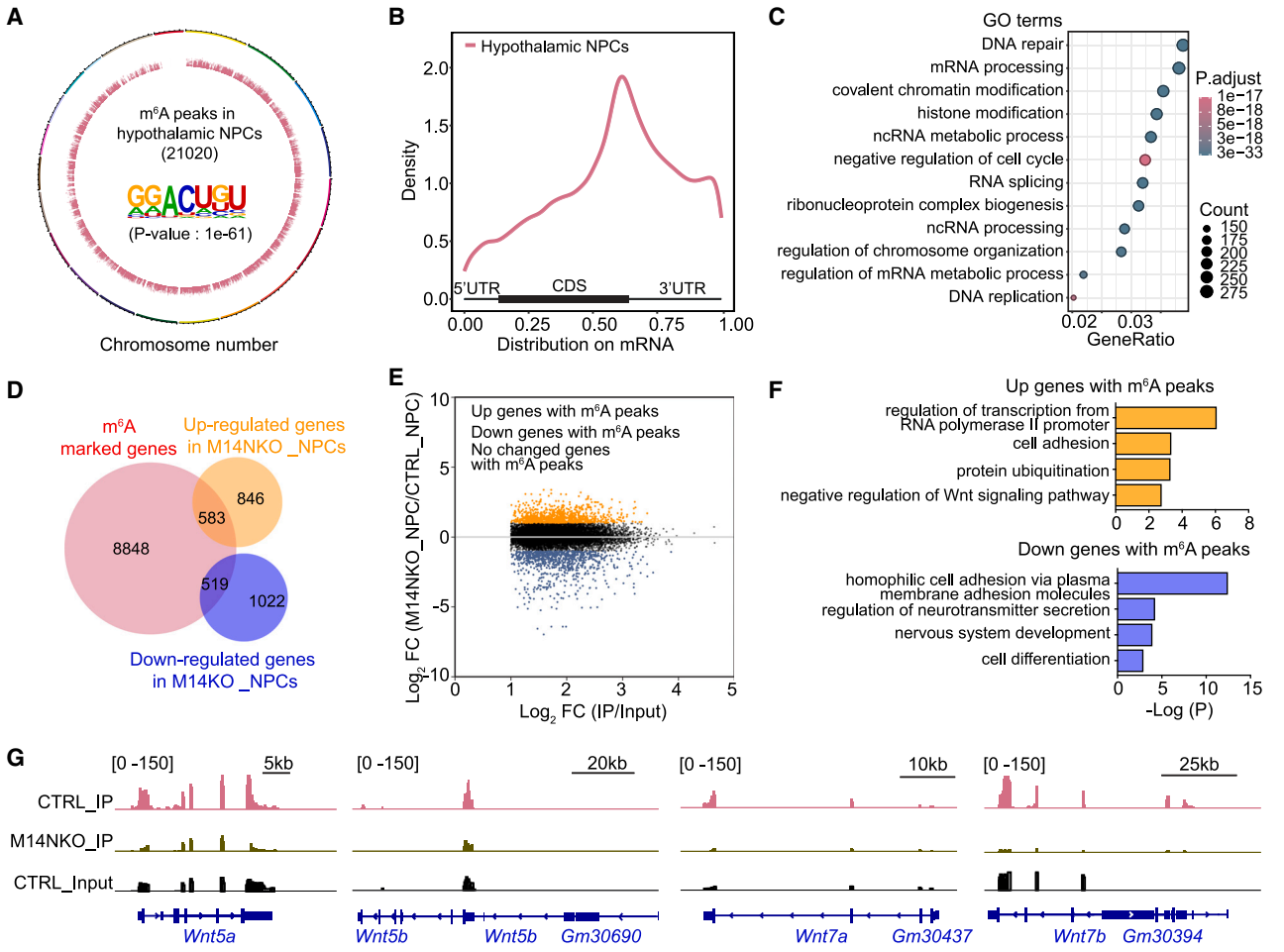

Figure 5. Altered expression of some m^{6}A-tagged transcripts in mouse embryonic hypothalamic NPCs

(A) Circos plots of the distribution patterns of m^{6}A peaks across chromosomes in mouse hypothalamic NPCs and consensus motifs on m^{6}A peaks identified.

(B) Metagene plots of the enrichment of m^{6}A peaks along the gene structure in mouse hypothalamic NPCs, divided into three non-overlapping segments: 5′ UTR, CDS, and 3′ UTR.

(C) GO pathway analysis for m^{6}A-tagged genes in mouse hypothalamic NPCs.

(D) Venn plot of m^{6}A-tagged genes in control NPCs and upregulated and downregulated genes in Mettl14 knockout NPCs compared with control NPCs.

(E) Scatterplot showing the abundance of m^{6}A (x axis) against gene expression changes in Mettl14 knockout NPCs compared with control NPCs (y axis) for each m^{6}A-tagged gene.

(F) GO pathway analysis for upregulated genes (top) and downregulated genes (bottom) in Mettl14 knockout NPCs that exhibited m^{6}A modifications in control NPCs.

(G) Visualization of m^{6}A peaks in representative Wnt family genes that exhibited downregulation in Mettl14 knockout NPCs.

See also Figure S3.

with the negative regulation of the Wnt signaling pathway in Mettl14 KO hypothalamic NPCs (Figure S3D) and m^{6}A modifications along the gene bodies of Wnt5a, Wnt5b, Wnt7a, and Wnt7b, all of which exhibited downregulation following Mettl14 deletion (Figures 5F, 5G, and S3E). Together, these analyses revealed the m^{6}A landscape and regulation of gene expression by Mettl14 in the embryonic hypothalamic NPCs.

Embryonic hypothalamic *Ythdc1* deletion impairs the generation of feeding-related neurons and leads to increased fat accumulation in adults

Mettl14 has functions independent of its m^{6}A methyltransferase activity.[63] To ascertain the direct involvement of m^{6}A signaling in regulating the generation of feeding-related neurons in the embryonic hypothalamus and body or fat mass in the adult, we performed genetic deletion experiments targeting additional components within the m^{6}A signaling pathway.

First, we deleted *Mettl3*, encoding another core component of the METTL3/MELLT14 m^{6}A methyltransferase complex, using NKX2.1-Cre::Mettl3$^{f/f}$ mice (named M3NKO mice). Both male and female NM3KO mice displayed accelerated weight gain relative to their Mettl3$^{f/f}$ CTRL counterparts and exhibited profound adult obesity (Figure S4A). Moreover, adult M3NKO mice exhibited reduced numbers of POMC$^+$ and OTP$^+$ neurons and a modest increase in the number of NeuN$^+$ cells in the ARC region compared with CTRL mice

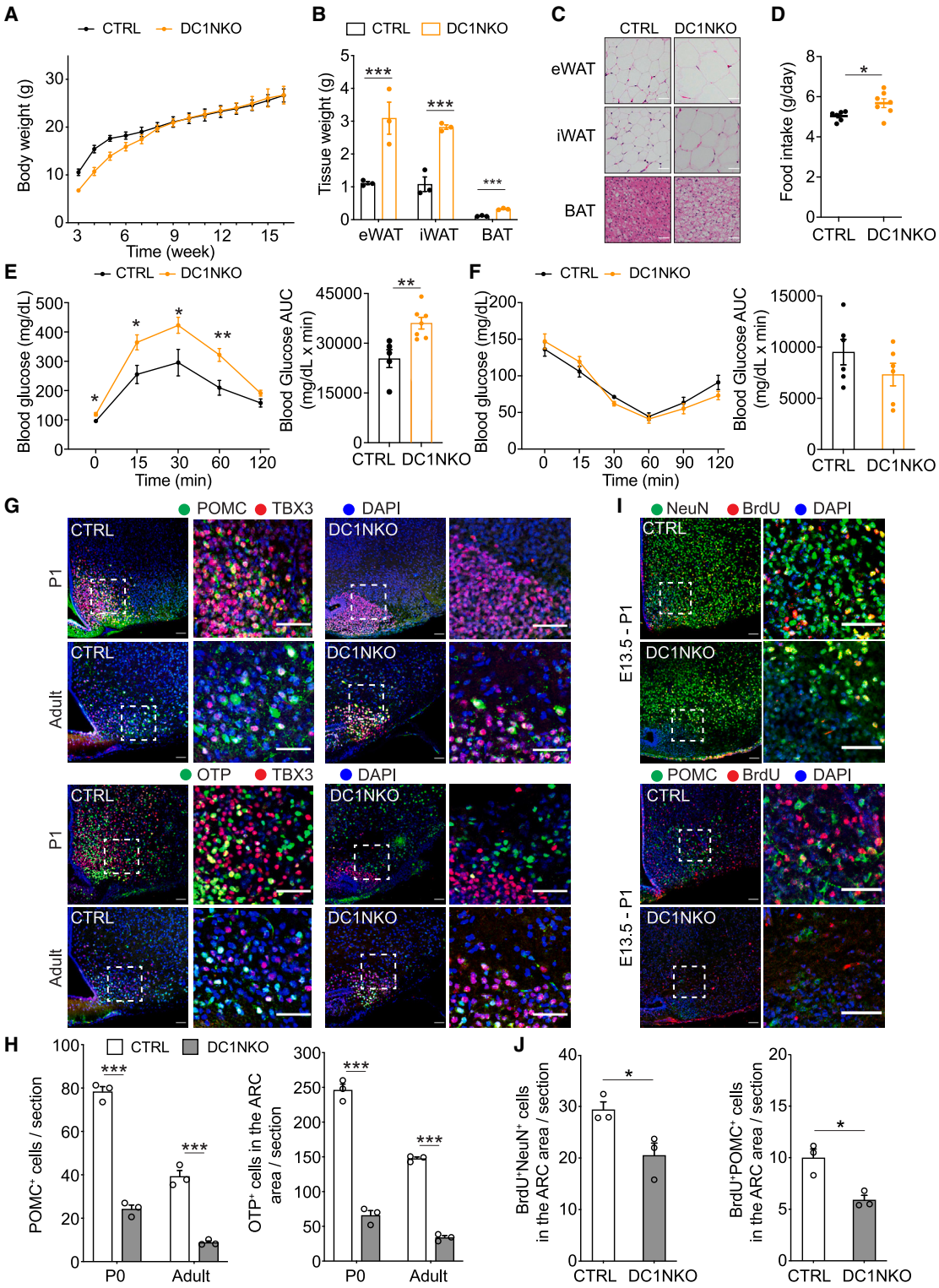

Figure 6. Embryonic hypothalamic *Ythdc1* deletion impairs the generation of feeding-related neurons and increases fat accumulation in adult mice

(A) Body weight of CTRL and DC1NKO female mice. Values represent mean ± SEM (n = 6/CTRL and 7/DC1NKO).

(B) Adipose depot weight of adult female CTRL and DC1NKO mice. Values represent mean ± SEM (n = 3 mice each group; ***p < 0.001, Student's t test).

(C) H&E staining of inguinal and gonadal adipose tissues of female CTRL and DC1NKO mice at 16 weeks. Scale bars: 50 μm.

(D) Food intake in 18-week-old female CTRL and DC1NKO mice. Same set of animals as in (A). Values represent mean ± SEM (***p < 0.001; Student's t test).

(legend continued on next page)

(Figures S4B–S4E), thus phenocopying the M14NKO mice (Figures 1A and 3D–3G).

Second, we deleted *Ythdf2*, encoding an m^{6}A reader known to regulate cortical neurogenesis via promoting mRNA decay,[64] using NKX2.1-Cre::Ythdf2$^{f/f}$ mice (named DF2NKO). The numbers of POMC$^+$, OTP$^+$, and NeuN$^+$ neurons were similar between adult DF2NKO mice and their Ythdf2$^{f/f}$ CTRL counterparts (Figures S5A–S5D). Adult DF2NKO mice also exhibited no change in their body weight compared with their CTRL counterparts (Figure S5E).

Third, we deleted *Ythdc1*, encoding a nuclear m^{6}A reader,[59] using NKX2.1-Cre::Ythdc1$^{f/f}$ mice (named DC1NKO). While adult DC1NKO mice showed no difference in body weight compared with their Ythdc1$^{f/f}$ CTRL littermates, they exhibited increased weight of the inguinal, gonadal, and brown fat depots, accompanied by adipocytes displaying greater hypertrophy compared with CTRL littermates (Figures 6A–6C and S5F). Similar to M14NKO mice (Figure 2A), adult DC1NKO mice exhibited increased food intake compared with CTRL mice (Figure 6D). Furthermore, adult DC1NKO mice displayed hyperglycemia but without concurrent insulin resistance compared with their CTRL littermates (Figures 6E and 6F). Also similar to M14NKO and M3NKO mice, DC1NKO mice exhibited reduced numbers of POMC$^+$ neurons and OTP$^+$ neurons in the ARC region compared with CTRL mice both at P0 and in the adult (Figures 6G and 6H). In contrast to M14NKO mice, the number of NeuN$^+$ neurons was decreased in the DC1NKO mice (Figures S5G and S5H). Birth-dating analysis further revealed a reduced generation of both NeuN$^+$BrdU$^+$ cells and POMC$^+$BrdU$^+$ cells in DC1NKO mice labeled at E13.5 (Figures 6I and 6J). These results indicate that Ythdc1, similar to Mettl14, plays a critical role in regulating the generation of feeding-related neurons during embryonic hypothalamic neurogenesis. However, adult DC1NKO mice displayed both overlapping and unique phenotypes compared with M14NKO mice, likely due to Ythdc1 functioning downstream of multiple m^{6}A methyltransferases, such as METTL16,[11] in addition to METTL3/14, and/or with additional functions.[59]

Together, multiple lines of mice with conditional deletions of m^{6}A signaling pathway components resulted in the decreased generation of feeding-related neurons in the ARC and an increase in body fat, underscoring the essential role of m^{6}A signaling in embryonic hypothalamic neurogenesis to prevent accumulation of excess fat or body weight in adult mice.

m^{6}A signaling regulates feeding-related neuron generation in human ARCOs

To examine whether the role of m^{6}A signaling in regulating the generation of feeding-related neurons in mice is conserved in humans, we used a human iPSC-derived brain subregion-specific ARCO model. Building upon our previous protocol with human iPSCs cultured on feeder cells,[65] we optimized a feeder-free protocol for generating more consistent human ARCOs (Figures 7A and S6A). The new method showcases three primary distinctions from the previous approach that remove several variables. First, human iPSCs were cultured on Matrigel-coated plates without feeder cells. Second, the transforming growth factor β (TGF-β) pathway inhibitor SB-431542, instead of A-83-01, was used for patterning, which reduced cell death during the process. Third, the mouse hypothalamic astrocyte-conditioned medium was replaced with CNTF. We first examined the early patterning of hypothalamic NPCs in ARCOs. qPCR analysis showed drastically increased mRNA expression levels of hypothalamic NPC markers *NKX2-1*, *RAX*, and *ASCL1* with a modest increase in the level of NESTIN compared with iPSCs at day 13 (Figure S6B). We confirmed the expression of NKX2.1 and MASH1 at the protein level by immunocytochemistry at day 12 (Figure S6C). Next, we examined the generation of various hypothalamic neuronal populations within ARCOs at days 20, 30, and 40 and found a gradual increase in the mRNA expression levels of hypothalamic neuronal markers *MAP2*, *MC4R*, *NPY*, and *TH* (Figure 7B). We also observed POMC$^+$, aMSH$^+$, OTP$^+$, and TH$^+$ cells by immunohistology from day 30 (Figures 7C, 7D, S6D, and S6E).

To identify m^{6}A-tagged transcripts in human hypothalamic NPCs, we performed m^{6}A-sequencing on day 12 ARCOs. We identified 34,130 m^{6}A peaks, predominantly featuring the GGAC consensus motif and located near stop codons (Figures 7E and S7E). GO analysis showed that m^{6}A-tagged transcripts were enriched in pathways related to cell differentiation, morphogenesis, covalent chromatin modifications, histone modifications, regulation of mRNA metabolic process, and RNA splicing (Figure 7F).

Next, we integrated transcripts with m^{6}A modifications in both mouse hypothalamic NPCs and human day 12 ARCOs. We identified 4,901 shared genes with m^{6}A modifications in their transcripts (Figure S7F). GO analysis of these conserved genes highlights pathways associated with chromatin remodeling, cell cycle regulation, DNA repair, RNA splicing, and the Wnt signaling pathway (Figure S7G). Similar to findings in mouse hypothalamic NPCs (Figure 5G), we observed m^{6}A modifications near the gene bodies of WNT5A, WNT5B, WNT7A, and WNT7B transcripts in human day 12 ARCOs (Figure S7H). Together, these analyses reveal conserved features of m^{6}A modifications in mouse and human hypothalamic NPCs.

Finally, we infected the day 11 ARCOs at the NPC stage with lentiviruses co-expressing GFP and either short hairpin RNA (shRNA) against *METTL14*, *YTHDC1*, or a scrambled shRNA control (Figures S6F–S6I and S7A). At day 40, quantification showed reduced percentages of GFP$^+$POMC$^+$NEUN$^+$ neurons and

(E) Summary of glucose tolerance test (left) and area under curve (AUC, right) in 20-week-old female CTRL and DC1NKO mice. Same set of animals as in (A). Values represent mean ± SEM (*p < 0.05, **p < 0.01; Student's t test).
(F) Summary of insulin tolerance test (left) and area above curve (AAC) (right) in 21-week-old female CTRL and DC1NKO mice. Same set of animals as in (A). Values represent mean ± SEM.
(G and H) Sample confocal images of POMC$^+$ and OTP$^+$ cells in the ARC region from CTRL and DC1NKO mice at P0 and adult stages (16 weeks) (G) and quantifications (H). Scale bars, 50 μm. Values represent mean ± SEM (n = 3 mice each group; *p < 0.05; Student's t test).
(I and J) Sample confocal images of NeuN$^+$BrdU$^+$ and POMC$^+$BrdU$^+$ cells in the ARC region from CTRL and DC1NKO mice at P1 with BrdU injected at embryonic day 13.5 (I) and quantifications (J). Scale bars, 50 μm. Values represent mean ± SEM (n = 3 mice each group; *p < 0.05; Student's t test).
See also Figures S4 and S5.

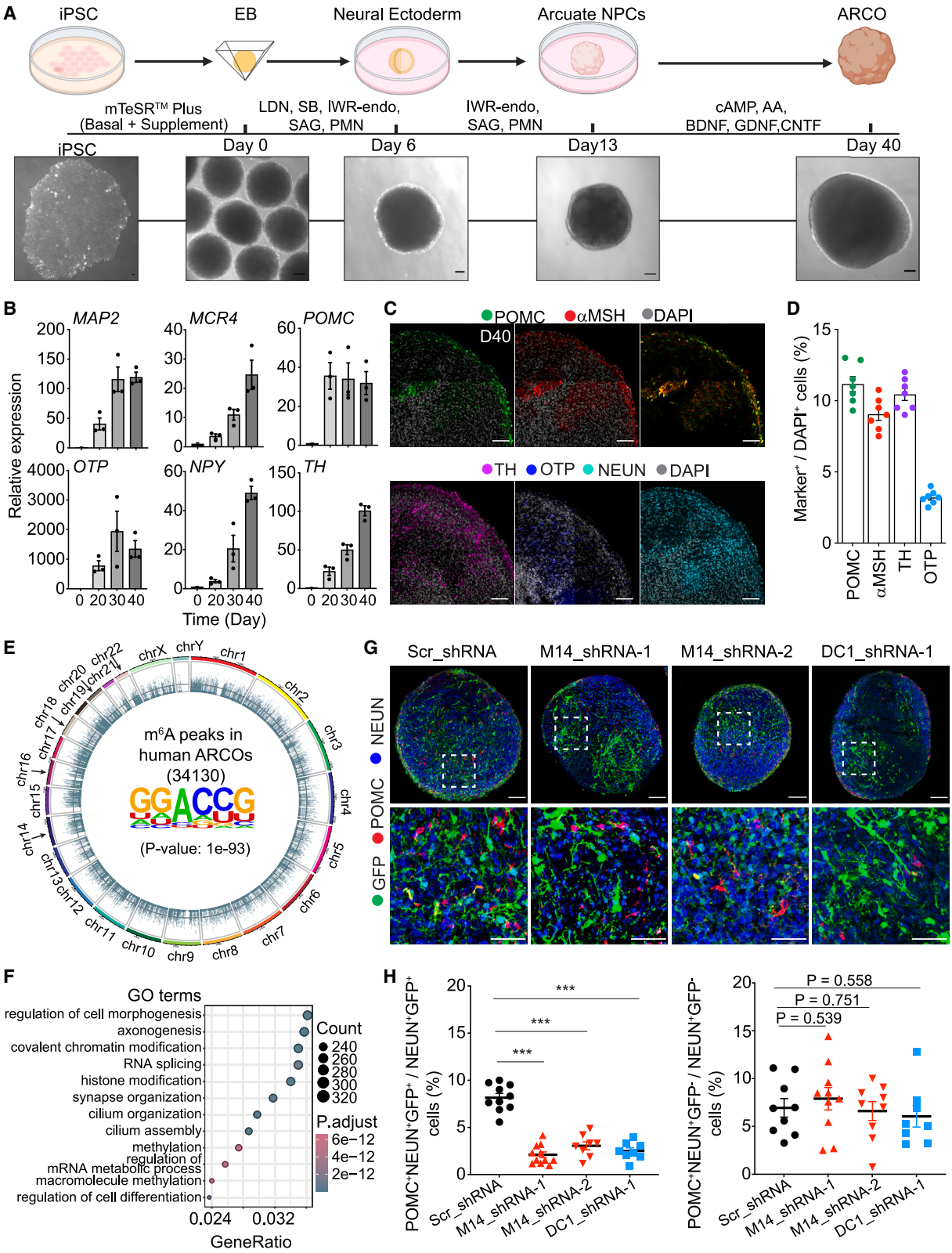

Figure 7. m⁶A signaling regulates feeding-related neuron generation in human ARCOs

(A) A schematic diagram of the protocol for generating ARCOs from human iPSCs (top) and sample bright-field images of iPSCs and ARCOs at different stages. Scale bars, 200 μm. ARCO, arcuate nucleus organoid; EB, embryonic body; LDN, LDN193189 (a derivative of dorsomorphin and an inhibitor of BMP type 1

(legend continued on next page)

GFP$^+$OPT$^+$NEUN$^+$ neurons among total GFP$^+$NEUN$^+$ neurons in ARCOs with either *METTL14* or *YTHDC1* knockdown compared with the scrambled shRNA control (Figures 7G, 7H, S7B, and S7C). Notably, the percentage of GFP$^-$POMC$^+$NEUN$^+$ neurons or GFP$^-$OPT$^+$NEUN$^+$ neurons among the GFP$^-$NEUN$^+$ neurons did not exhibit any difference across the groups, indicating a cell-autonomous effect (Figures 7H and S7C). Similar as in M14NKO mice (Figure 3C), we observed decreased expression of POMC and NPY in fluorescence-activated cell sorting (FACS)-purified GFP$^+$ cells in ARCOs with *METTL14* or *YTHDC1* knockdown compared with the scrambled shRNA control (Figure S7D). Together, these results suggest that, as in mice, m^{6}A signaling, mediated by METTL14 and YTHDC1, plays a pivotal role in generating human feeding-related neurons.

DISCUSSION

Using multiple genetic mouse models, we showed that conditional deletion of two m^{6}A writers, Mettl14 and Mettl3, and one m^{6}A reader, Ythdc1, in the embryonic hypothalamus all lead to decreased generation of feeding-related neurons in the ARC region of the hypothalamus and increased body or fat mass in adult. Both M14NKO and DC1NKO mice also showed increased food intake, hyperglycemia, and adipocyte hypertrophy. Furthermore, we showed a conserved role of m^{6}A signaling in the generation of human feeding-related neurons using an improved human iPSC-derived brain subregion-specific ARCO model. Together, our study reveals the developmental basis and cellular mechanism of epitranscriptomic m^{6}A regulation of food intake and body or fat mass.

Global overexpression of FTO in mice led to heightened body and fat mass as well as increased food intake.[44] Conversely, deletion of FTO globally or in the nervous system in mice leads to postnatal growth retardation, significant reductions in adipose tissue, lean body mass, and increased energy expenditure.[66] Given that m^{6}A$_m$ is the preferred demethylation substrate of FTO, compared with m^{6}A,[45] whether m^{6}A signaling is involved in regulating food intake and body weight was not previously clear. In our study, we observed that M14NKO mice were smaller than their control littermates during the weaning period. This finding is in line with Nestin-Cre-based Mettl14 cKO mice, which also showed a smaller size after birth but die around P25.[20] Subsequently, M14NKO mice exhibited an increased body weight, eventually developing significant obesity in adulthood, accompanied by dysregulated glucose homeostasis likely due to a notable increase in their food intake, which is similar to global FTO overexpression mice.[44] Importantly, deletion of another m^{6}A writer, Mettl3, leads to nearly identical phenotypes, and deletion of the m^{6}A reader, Ythdc1, also leads to increased fat mass and food intake. Together, these multiple lines of evidence from several genetic manipulations firmly establish a critical role for epitrancriptomic m^{6}A regulation of food intake and body or fat mass in mice.

Previous studies have established that m^{6}A modifications play crucial roles in regulating the development of the cortex and cerebellum.[18,20,22] For instance, Mettl14 deletion in cortical radial glial cells in Nestin-Cre::Mettl14$^{f/f}$ mice leads to a prolonged tempo of sequential generation of upper-layer and deep-layer cortical neurons.[20,22] We observed a decreased number of multiple feeding-related neurons in the hypothalamus of M14NKO mice, which may explain a significant increase in food intake observed in M14NKO mice. Notably, both POMC$^+$ and AGRP$^+$ neurons were decreased in M14NKO mice. These neurons are known to play opposite roles in regulating food intake and energy expenditure, with POMC$^+$ neurons suppressing appetite[30] and AGRP$^+$ neurons stimulating appetite.[29,56] Consistent with our results, mice deficient in both *Agrp* and *Pomc* exhibit a phenotype similar to *Pomc*-deficient mice alone, showing comparable levels of hyperphagia and obesity.[28] Our BrdU birth-dating experiments showed a delay in the production of NeuN$^+$ cells in our M14NKO mouse model (Figures 4B and 4C), which mirrors the delayed cortical neurogenesis observed in Nestin-Cre::Mettl14$^{f/f}$ mice.[20,22] However, in contrast to cortical neurogenesis, where the neuronal subtype fate is not altered in Nestin-Cre::Mettl14$^{f/f}$ mice,[20] neuronal subtype fate is affected during ARC neurogenesis, as shown by a decreased number of POMC$^+$ and other feeding-related neurons and an increased number of some other neuronal subtypes in the absence of changes in the total number of neurons in the ARC of M14NKO mice (Figure 3B). Recent clonal lineage-tracing experiments have shown that a single NPC is capable of generating multiple neuronal subtypes in either the embryonic cortex or ARC in mice, yet neuronal subtype generation in the cortex follows a progressive and fixed sequence, whereas it is stochastic in the ARC.[25,67,68] It is possible that m^{6}A-dependent prolonging of the neurogenesis tempo affects the fate choice in the stochastic neurogenesis mode but not in the sequential progressive neurogenesis mode.

We further established an *in vitro* system with Mettl14 KO hypothalamic NPCs that replicates the phenotype of deficits in the generation of feeding-related neurons observed *in vivo*, allowing for exploration into the m^{6}A-related mechanisms. By integrating

receptors ALK2 and ALK3); SB, SB431542 (an inhibitor of TGF-β type 1 receptors ALK5, ALK4, and ALK7); SAG, smoothened agonist; PMN, purmorphamine (an activator of the SHH pathway).

(B) Summary of qPCR analysis of marker gene expression levels in iPSCs and ARCOs at day 20, 30, and 40. Values represent mean ± SEM (n = 4–5 organoids).

(C and D) Sample confocal images of immunostaining for NEUN, POMC, αMSH, TH, and OTP in ARCOs at 40 days (C) and quantification of percentages of POMC$^+$, αMSH$^+$, TH$^+$, and OTP$^+$ cells among DAPI$^+$ cells (D). Scale bar, 50 μm (C). Each dot represents data from each organoid (D). Values represent mean ± SEM (n = 7 organoids).

(E) Circos plots of the distribution patterns of m^{6}A peaks across chromosomes in day 12 human ARCOs and consensus motifs on m^{6}A peaks identified.

(F) GO pathway analysis for m^{6}A-tagged genes in day 12 human ARCOs.

(G and H) Sample confocal images of immunostaining for NEUN, POMC, and GFP in day 40 ARCOs upon infection with lentivirus co-expressing GFP and scrambled shRNA or shRNA for METTL14 or YTHDC1 at day 11 and analysis at day 40 (G). Scale bars, 100 μm. Also shown are quantifications of percentages of POMC$^+$NEUN$^+$GFP$^+$ neurons among all NEUN$^+$GFP$^+$ neurons (left) and percentages of POMC$^+$NEUN$^+$GFP$^-$ neurons among all NEUN$^+$GFP$^-$ neurons (right) in day 40 ARCOs (H). Values represent mean ± SEM (n = 5 organoids; ***p < 0.001; Student's t test).

See also Figures S6 and S7 and Table S2.

analysis of m^{6}A-tagged transcripts and changes in gene expression observed in Mettl14-deleted hypothalamic NPCs using m^{6}A-seq and RNA-seq, we uncovered many downregulated genes with m^{6}A modifications that are related to nervous system development and cell differentiation, including several components of the Wnt pathway (Wnt5a, Wnt5b, Wnt7a, and Wnt7b) (Figure 5F), which could potentially participate in the m^{6}A-mediated regulation of feeding-related neuron generation, paving the way for future studies.

A previous study has shown that m^{6}A signaling regulates cortical neurogenesis in part via the mRNA decay mechanism involving the m^{6}A reader Ythdf2.[64] While we also observed a shared phenotype of regulation of the tempo of hypothalamic neurogenesis by m^{6}A signaling as previously reported in cortical neurogenesis,[20,22] deletion of Ythdf2 had no impact on the generation of POMC+ neurons or body weight (Figures S6A–S6E). Instead, in line with our finding regarding m^{6}A-tagged transcripts linked to RNA splicing (Figure 5C), the deletion of m^{6}A reader Ythdc1 resembles decreased generation of POMC$^+$ neurons observed in M14NKO and M3NKO mice (Figures S5A–S5D, 6G, and 6H). Birth-dating analysis further corroborated these findings, revealing a decline in the number of BrdU$^+$POMC$^+$ cells in DC1NKO mice that was comparable to that observed in M14NKO mice (Figures 4A–4E, 6I, and 6J). In contrast to M14NKO mice, we found a decreased number of NeuN$^+$ cells in DC1NKO mice (Figures 3F, 3G, S5G, and S5H). The impact on the overall number of neurons may contribute to the observed accumulation of adipose tissue without changes in body weight in DC1NKO mice (Figures 6A–6C). The differential effects between Mettl14 and Ythdc1 conditional deletion are not particularly surprising, as Ythdc1 functions downstream of multiple m^{6}A methyltransferases, such as METTL16[11] in addition to METTL3/14, and it could have additional functions independent of m^{6}A signaling.[59] All together, these studies revealed that m^{6}A writers and its readers exert both shared and differential regulatory influences on neurogenesis in various sub-regions of the embryonic brain.

Several human neurodevelopmental, neurodegenerative, and neuropsychiatric disorders have been linked to defects in m^{6}A modifications.[1] Recently, brain organoids have gained prominence as a valuable model for studying human brain development and disorders.[48,49] We optimized our previous protocol[65] for the generation of brain subregion-specific ARCOs from feeder-free human iPSCs. Our model exhibits strong expression of hypothalamic NPC markers and transcription factors enriched in a diverse range of hypothalamic neuronal populations, including *NKX2-1*, *ASCL1*, *POMC*, *TH*, and *OTP* (Figures 7B and S6B). In comparison to our prior ARCO models, our current approach stands out for its ease of handling and the reduced variability observed among individual organoids (Figure S6A). Our m^{6}A-sequencing on day 12 ARCOs revealed conserved m6A modifications in transcripts associated with chromatin remodeling, cell cycle regulation, DNA repair, RNA splicing, and the Wnt signaling pathway in mouse and human hypothalamic NPCs (Figure S7G). To avoid confounds from the potential regulation by m^{6}A signaling at the iPSC stage, we utilized lentivirus-expressed shRNA to reduce the expression of *METTL14* or *YTHDC1* to approximately 30% after patterning human iPSCs to hypothalamic NPCs. Our findings indicate that both METTL14 and YTHDC1 are necessary for generation of feeding-related human hypothalamic neurons, mirroring observations in mouse models. These findings provide additional support for the conserved impact of m^{6}A regulation on mammalian hypothalamic neuron generation.

Limitations of the study

First, our study showed an essential role of m^{6}A signaling in hypothalamic neurogenesis in mice using NKX2-1 Cre, which has been extensively employed in studies focusing on hypothalamic development and function.[50–52] However, this Cre line is also active in interneurons, as well as in the lung and thyroid gland. Therefore, we cannot rule out the contribution of other cell types to the observed adult obesity and related phenotypes. On the other hand, we confirmed the critical role of m^{6}A signaling in generation of POMC$^+$ neurons from both mouse and human hypothalamic NPCs *in vitro*. Second, we performed selected metabolic analysis in some of the genetically modified mice. More detailed analysis may reveal additional insight. Third, our cellular and molecular studies focused on the ARC region of the hypothalamus. Neurogenesis in other hypothalamic nuclei could also be affected but that remains to be characterized. Fourth, our study also revealed differentially expressed genes in the remaining feeding-related neurons with defective m^{6}A signaling. The potential contribution of defective m^{6}A signaling in these feeding-related neurons to adult obesity remains to be determined. Fifth, while both M14NKO and DC1NKO mice exhibited increased fat mass and reduced generation of hypothalamic neurons, M14NKO mice exhibited increased body weight, whereas DC1NKO mice did not. Such differences are likely due to Ythdc1 functioning downstream of multiple m^{6}A methyltranferases with potential additional functions,[11] but the detailed mechanism remains to be explored. Sixth, our study revealed a molecular mechanism of hypothalamic neurogenesis involving m^{6}A signaling and a cellular mechanism for the obesity phenotype involving the reduced generation of feeding-related neurons. We also identified many m^{6}A-tagged transcripts in hypothalamic NPCs that exhibit differential expression upon Mettl14 deletion. However, the exact molecular targets of m^{6}A-containing transcripts involved in hypothalamic neurogenesis require further investigation, and it is likely that many genes could be involved.

RESOURCE AVAILABILITY

Lead contact

Further information and requests for resources and reagents should be directed to and will be fulfilled by the lead contact, Dr. Hongjun Song (shongjun@pennmedicine.upenn.edu).

Material availability

All unique/stable reagents and biological material generated in this study are available from the lead contact, Dr. Hongjun Song (shongjun@pennmedicine.upenn.edu), with a completed material transfer agreement.

Data and code availability

- The sequencing data reported in this study are deposited in GEO, including single-cell RNA-seq (GEO: GSE267200), bulk RNA-seq (GEO: GSE267199), and mouse and human m^{6}A-seq (GEO: GSE267202 and GSE289462).
- No original code was generated in this study.
- Any additional information required to reanalyze the data reported in this paper is available from the lead contact upon request.

ACKNOWLEDGMENTS

We thank members of Ming and Song laboratories and Kimberly Christian for comments and suggestions and B. Temsamrit, E. LaNoce, A. Angelucci, and G. Alepa for laboratory support. We thank Richard A. Flavell and Brian C. Capell for providing the Mettl3$^{f/f}$ mice, the Rodent Metabolic Phenotyping Core at the University of Pennsylvania Institute for Diabetes, Obesity, & Metabolism for some metabolic cage analyses, and M.S. Haney for support. This work was supported by grants from the National Institutes of Health (R35NS097370 and R35NS137480 to G.-l.M., R35NS116843 to H.S., and RM1HG008935 to C.H. and H.S.) and from the Dr. Miriam and Sheldon G. Adelson Medical Research Foundation (to G.-l.M. and D.H.G.).

AUTHOR CONTRIBUTIONS

Y.S. led the project and contributed to all aspects of the study analysis. Y.S. and T.M. contributed to immunostaining analysis. S.Z.H.W. initially identified the obesity phenotype of M14NKO mice. Y.S. and F.Z. contributed to GTT and ITT analysis for NDC1KO mice. Y.S., Q.W., R.K., and D.G. contributed to m^{6}A and RNA-seq. C.H. and J.W. contributed Ythdf2$^{f/f}$ mice and Ythdc1$^{f/f}$ mice, respectively. Y.S., G.-l.M., and H.S. conceived the project and wrote the manuscript.

DECLARATION OF INTERESTS

G-l.M. is a member of the advisory board of *Cell Stem Cell*.

STAR★METHODS

Detailed methods are provided in the online version of this paper and include the following:

- KEY RESOURCES TABLE
- EXPERIMENTAL MODEL AND STUDY PARTICIPANT DETAILS
  - Animals
  - Primary Mouse Hypothalamic NPC Culture
  - Human Induced Pluripotent Stem Cells Culture
- METHOD DETAILS
  - Body Weight, Food Intake and Body Metabolic Analysis
  - Glucose and Insulin Test
  - H&E Staining
  - Tissue Microdissection and Dissociation
  - Single-cell RNA-Seq Library Preparation and Sequencing
  - Single-cell RNA-seq Data Analysis
  - Generation and Differentiation of Mettl14 Knockout Hypothalamic NPCs
  - RNA Isolation and qPCR
  - RNA-seq, m^{6}A-seq and Data Analyses
  - Tissue and Organoid Preparation and Sectioning
  - Immunohistology and Confocal Imaging
  - BrdU Birth-Dating Analysis
  - Generation of ARCOs from Feeder-free Human iPSCs
  - shRNA Lentivirus Production and Infection of Organoids
  - Protein Extraction and Western Blot
- QUANTIFICATION AND STATISTICAL ANALYSIS

SUPPLEMENTAL INFORMATION

Supplemental information can be found online at https://doi.org/10.1016/j.stem.2025.02.011.

Received: July 6, 2024
Revised: December 7, 2024
Accepted: February 24, 2025
Published: March 19, 2025

REFERENCES

1. Zhang, F., Ignatova, V.V., Ming, G.L., and Song, H. (2024). Advances in brain epitranscriptomics research and translational opportunities. Mol. Psychiatry *29*, 449–463. https://doi.org/10.1038/s41380-023-02339-x.
2. Li, X., Xiong, X., and Yi, C. (2016). Epitranscriptome sequencing technologies: decoding RNA modifications. Nat. Methods *14*, 23–31. https://doi.org/10.1038/nmeth.4110.
3. Desrosiers, R.C., Friderici, K.H., and Rottman, F.M. (1975). Characterization of Novikoff hepatoma mRNA methylation and heterogeneity in the methylated 5' terminus. Biochemistry *14*, 4367–4374.
4. Roundtree, I.A., Evans, M.E., Pan, T., and He, C. (2017). Dynamic RNA Modifications in Gene Expression Regulation. Cell *169*, 1187–1200. https://doi.org/10.1016/j.cell.2017.05.045.
5. Bokar, J.A., Rath-Shambaugh, M.E., Ludwiczak, R., Narayan, P., and Rottman, F. (1994). Characterization and partial purification of mRNA N6-adenosine methyltransferase from HeLa cell nuclei. Internal mRNA methylation requires a multisubunit complex. J. Biol. Chem. *269*, 17697–17704.
6. Bokar, J.A., Shambaugh, M.E., Polayes, D., Matera, A.G., and Rottman, F.M. (1997). Purification and cDNA cloning of the AdoMet-binding subunit of the human mRNA (N6-adenosine)-methyltransferase. RNA *3*, 1233–1247.
7. Liu, J., Yue, Y., Han, D., Wang, X., Fu, Y., Zhang, L., Jia, G., Yu, M., Lu, Z., Deng, X., et al. (2014). A METTL3-METTL14 complex mediates mammalian nuclear RNA N6-adenosine methylation. Nat. Chem. Biol. *10*, 93–95. https://doi.org/10.1038/nchembio.1432.
8. Ping, X.L., Sun, B.F., Wang, L., Xiao, W., Yang, X., Wang, W.J., Adhikari, S., Shi, Y., Lv, Y., Chen, Y.S., et al. (2014). Mammalian WTAP is a regulatory subunit of the RNA N6-methyladenosine methyltransferase. Cell Res. *24*, 177–189. https://doi.org/10.1038/cr.2014.3.
9. Schwartz, S., Mumbach, M.R., Jovanovic, M., Wang, T., Maciag, K., Bushkin, G.G., Mertins, P., Ter-Ovanesyan, D., Habib, N., Cacchiarelli, D., et al. (2014). Perturbation of m6A writers reveals two distinct classes of mRNA methylation at internal and 5' sites. Cell Rep. *8*, 284–296. https://doi.org/10.1016/j.celrep.2014.05.048.
10. Wang, Y., Li, Y., Toth, J.I., Petroski, M.D., Zhang, Z., and Zhao, J.C. (2014). N6-methyladenosine modification destabilizes developmental regulators in embryonic stem cells. Nat. Cell Biol. *16*, 191–198. https://doi.org/10.1038/ncb2902.
11. Warda, A.S., Kretschmer, J., Hackert, P., Lenz, C., Urlaub, H., Höbartner, C., Sloan, K.E., and Bohnsack, M.T. (2017). Human METTL16 is a N6-methyladenosine (m6A) methyltransferase that targets pre-mRNAs and various non-coding RNAs. EMBO Rep. *18*, 2004–2014. https://doi.org/10.15252/embr.201744940.
12. Fu, Y., Jia, G., Pang, X., Wang, R.N., Wang, X., Li, C.J., Smemo, S., Dai, Q., Bailey, K.A., Nobrega, M.A., et al. (2013). FTO-mediated formation of N6-hydroxymethyladenosine and N6-formyladenosine in mammalian RNA. Nat. Commun. *4*, 1798. https://doi.org/10.1038/ncomms2822.
13. Zheng, G., Dahl, J.A., Niu, Y., Fedorcsak, P., Huang, C.M., Li, C.J., Vågbø, C.B., Shi, Y., Wang, W.L., Song, S.H., et al. (2013). ALKBH5 is a mammalian RNA demethylase that impacts RNA metabolism and mouse fertility. Mol. Cell *49*, 18–29. https://doi.org/10.1016/j.molcel.2012.10.015.
14. Flamand, M.N., Tegowski, M., and Meyer, K.D. (2023). The Proteins of mRNA Modification: Writers, Readers, and Erasers. Annu. Rev. Biochem. *92*, 145–173. https://doi.org/10.1146/annurev-biochem-052521-035330.
15. Li, L., Zang, L., Zhang, F., Chen, J., Shen, H., Shu, L., Liang, F., Feng, C., Chen, D., Tao, H., et al. (2017). Fat mass and obesity-associated (FTO) protein regulates adult neurogenesis. Hum. Mol. Genet. *26*, 2398–2411. https://doi.org/10.1093/hmg/ddx128.
16. Ma, C., Chang, M., Lv, H., Zhang, Z.W., Zhang, W., He, X., Wu, G., Zhao, S., Zhang, Y., Wang, D., et al. (2018). RNA m6A methylation participates in regulation of postnatal development of the mouse cerebellum. Genome Biol. *19*, 68. https://doi.org/10.1186/s13059-018-1435-z.

17. Shi, H., Zhang, X., Weng, Y.L., Lu, Z., Liu, Y., Lu, Z., Li, J., Hao, P., Zhang, Y., Zhang, F., et al. (2018). m6A facilitates hippocampus-dependent learning and memory through YTHDF1. Nature *563*, 249–253. https://doi.org/10.1038/s41586-018-0666-1.

18. Wang, C.X., Cui, G.S., Liu, X., Xu, K., Wang, M., Zhang, X.X., Jiang, L.Y., Li, A., Yang, Y., Lai, W.Y., et al. (2018). METTL3-mediated m6A modification is required for cerebellar development. PLoS Biol. *16*, e2004880. https://doi.org/10.1371/journal.pbio.2004880.

19. Weng, Y.L., Wang, X., An, R., Cassin, J., Vissers, C., Liu, Y., Liu, Y., Xu, T., Wang, X., Wong, S.Z.H., et al. (2018). Epitranscriptomic m(6)A Regulation of Axon Regeneration in the Adult Mammalian Nervous System. Neuron *97*, 313–325.e6. https://doi.org/10.1016/j.neuron.2017.12.036.

20. Yoon, K.J., Ringeling, F.R., Vissers, C., Jacob, F., Pokrass, M., Jimenez-Cyrus, D., Su, Y., Kim, N.S., Zhu, Y., Zheng, L., et al. (2017). Temporal Control of Mammalian Cortical Neurogenesis by m6A Methylation. Cell *171*, 877–889.e17. https://doi.org/10.1016/j.cell.2017.09.003.

21. Edens, B.M., Vissers, C., Su, J., Arumugam, S., Xu, Z., Shi, H., Miller, N., Rojas Ringeling, F., Ming, G.L., He, C., et al. (2019). FMRP Modulates Neural Differentiation through m(6)A-Dependent mRNA Nuclear Export. Cell Rep. *28*, 845–854.e5. https://doi.org/10.1016/j.celrep.2019.06.072.

22. Niu, F., Che, P., Yang, Z., Zhang, J., Yang, L., Zhuang, M., Ou, X., and Ji, S.J. (2022). m6A regulation of cortical and retinal neurogenesis is mediated by the redundant m6A readers YTHDFs. iScience *25*, 104908. https://doi.org/10.1016/j.isci.2022.104908.

23. Saper, C.B., and Lowell, B.B. (2014). The hypothalamus. Curr. Biol. *24*, R1111–R1116. https://doi.org/10.1016/j.cub.2014.10.023.

24. Sternson, S.M. (2013). Hypothalamic survival circuits: blueprints for purposive behaviors. Neuron *77*, 810–824. https://doi.org/10.1016/j.neuron.2013.02.018.

25. Ma, T., Wong, S.Z.H., Lee, B., Ming, G.L., and Song, H. (2021). Decoding neuronal composition and ontogeny of individual hypothalamic nuclei. Neuron *109*, 1150–1167.e6. https://doi.org/10.1016/j.neuron.2021.01.026.

26. Romanov, R.A., Tretiakov, E.O., Kastriti, M.E., Zupancic, M., Häring, M., Korchynska, S., Popadin, K., Benevento, M., Rebernik, P., Lallemend, F., et al. (2020). Molecular design of hypothalamus development. Nature *582*, 246–252. https://doi.org/10.1038/s41586-020-2266-0.

27. Swaab, D.F., Hofman, M.A., Lucassen, P.J., Purba, J.S., Raadsheer, F.C., and Van de Nes, J.A. (1993). Functional neuroanatomy and neuropathology of the human hypothalamus. Anat. Embryol. *187*, 317–330. https://doi.org/10.1007/BF00185889.

28. Corander, M.P., Rimmington, D., Challis, B.G., O'rahilly, S., and Coll, A.P. (2011). Loss of agouti-related peptide does not significantly impact the phenotype of murine POMC deficiency. Endocrinology *152*, 1819–1828. https://doi.org/10.1210/en.2010-1450.

29. Gropp, E., Shanabrough, M., Borok, E., Xu, A.W., Janoschek, R., Buch, T., Plum, L., Balthasar, N., Hampel, B., Waisman, A., et al. (2005). Agouti-related peptide-expressing neurons are mandatory for feeding. Nat. Neurosci. *8*, 1289–1291. https://doi.org/10.1038/nn1548.

30. Yaswen, L., Diehl, N., Brennan, M.B., and Hochgeschwender, U. (1999). Obesity in the mouse model of pro-opiomelanocortin deficiency responds to peripheral melanocortin. Nat. Med. *5*, 1066–1070. https://doi.org/10.1038/12506.

31. Bedont, J.L., Newman, E.A., and Blackshaw, S. (2015). Patterning, specification, and differentiation in the developing hypothalamus. Wiley Interdiscip. Rev. Dev. Biol. *4*, 445–468. https://doi.org/10.1002/wdev.187.

32. Markakis, E.A. (2002). Development of the neuroendocrine hypothalamus. Front. Neuroendocrinol. *23*, 257–291. https://doi.org/10.1016/s0091-3022(02)00003-1.

33. Zhang, Y.H., Xu, M., Shi, X., Sun, X.L., Mu, W., Wu, H., Wang, J., Li, S., Su, P., Gong, L., et al. (2021). Cascade diversification directs generation of neuronal diversity in the hypothalamus. Cell Stem Cell *28*, 1483–1499.e8. https://doi.org/10.1016/j.stem.2021.03.020.

34. Zhou, X., Lu, Y., Zhao, F., Dong, J., Ma, W., Zhong, S., Wang, M., Wang, B., Zhao, Y., Shi, Y., et al. (2022). Deciphering the spatial-temporal transcriptional landscape of human hypothalamus development. Cell Stem Cell *29*, 328–343.e5. https://doi.org/10.1016/j.stem.2021.11.009.

35. Swaab, D.F. (1997). Prader-Willi syndrome and the hypothalamus. Acta Paediatr. Suppl. *423*, 50–54. https://doi.org/10.1111/j.1651-2227.1997.tb18369.x.

36. Liu, J., Li, K., Cai, J., Zhang, M., Zhang, X., Xiong, X., Meng, H., Xu, X., Huang, Z., Peng, J., et al. (2020). Landscape and Regulation of m6A and m6Am Methylome across Human and Mouse Tissues. Mol. Cell *77*, 426–440.e6. https://doi.org/10.1016/j.molcel.2019.09.032.

37. Yang, Y., Shen, F., Huang, W., Qin, S., Huang, J.T., Sergi, C., Yuan, B.F., and Liu, S.M. (2019). Glucose Is Involved in the Dynamic Regulation of m6A in Patients With Type 2 Diabetes. J. Clin. Endocrinol. Metab. *104*, 665–673. https://doi.org/10.1210/jc.2018-00619.

38. Zhong, X., Yu, J., Frazier, K., Weng, X., Li, Y., Cham, C.M., Dolan, K., Zhu, X., Hubert, N., Tao, Y., et al. (2018). Circadian Clock Regulation of Hepatic Lipid Metabolism by Modulation of m6A mRNA Methylation. Cell Rep. *25*, 1816–1828.e4. https://doi.org/10.1016/j.celrep.2018.10.068.

39. Claussnitzer, M., Dankel, S.N., Kim, K.H., Quon, G., Meuleman, W., Haugen, C., Glunk, V., Sousa, I.S., Beaudry, J.L., Puviindran, V., et al. (2015). FTO Obesity Variant Circuitry and Adipocyte Browning in Humans. N. Engl. J. Med. *373*, 895–907. https://doi.org/10.1056/NEJMoa1502214.

40. Fawcett, K.A., and Barroso, I. (2010). The genetics of obesity: FTO leads the way. Trends Genet. *26*, 266–274. https://doi.org/10.1016/j.tig.2010.02.006.

41. Smemo, S., Tena, J.J., Kim, K.H., Gamazon, E.R., Sakabe, N.J., Gómez-Marín, C., Aneas, I., Credidio, F.L., Sobreira, D.R., Wasserman, N.F., et al. (2014). Obesity-associated variants within FTO form long-range functional connections with IRX3. Nature *507*, 371–375. https://doi.org/10.1038/nature13138.

42. Stratigopoulos, G., LeDuc, C.A., Cremona, M.L., Chung, W.K., and Leibel, R.L. (2011). Cut-like homeobox 1 (CUX1) regulates expression of the fat mass and obesity-associated and retinitis pigmentosa GTPase regulator-interacting protein-1-like (RPGRIP1L) genes and coordinates leptin receptor signaling. J. Biol. Chem. *286*, 2155–2170. https://doi.org/10.1074/jbc.M110.188482.

43. Stratigopoulos, G., Padilla, S.L., LeDuc, C.A., Watson, E., Hattersley, A.T., McCarthy, M.I., Zeltser, L.M., Chung, W.K., and Leibel, R.L. (2008). Regulation of Fto/Ftm gene expression in mice and humans. Am. J. Physiol. Regul. Integr. Comp. Physiol. *294*, R1185–R1196. https://doi.org/10.1152/ajpregu.00839.2007.

44. Church, C., Moir, L., McMurray, F., Girard, C., Banks, G.T., Teboul, L., Wells, S., Brüning, J.C., Nolan, P.M., Ashcroft, F.M., et al. (2010). Overexpression of Fto leads to increased food intake and results in obesity. Nat. Genet. *42*, 1086–1092. https://doi.org/10.1038/ng.713.

45. Mauer, J., Luo, X., Blanjoie, A., Jiao, X., Grozhik, A.V., Patil, D.P., Linder, B., Pickering, B.F., Vasseur, J.J., Chen, Q., et al. (2017). Reversible methylation of m6Am in the 5′ cap controls mRNA stability. Nature *541*, 371–375. https://doi.org/10.1038/nature21022.

46. Lancaster, M.A., and Knoblich, J.A. (2014). Organogenesis in a dish: modeling development and disease using organoid technologies. Science *345*, 1247125. https://doi.org/10.1126/science.1247125.

47. Paşca, S.P. (2018). The rise of three-dimensional human brain cultures. Nature *553*, 437–445. https://doi.org/10.1038/nature25032.

48. Qian, X., Song, H., and Ming, G.L. (2019). Brain organoids: advances, applications and challenges. Development *146*, dev166074. https://doi.org/10.1242/dev.166074.

49. Zhang, Z., Wang, X., Park, S., Song, H., and Ming, G.L. (2023). Development and Application of Brain Region-Specific Organoids for Investigating Psychiatric Disorders. Biol. Psychiatry *93*, 594–605. https://doi.org/10.1016/j.biopsych.2022.12.015.

50. Orquera, D.P., Tavella, M.B., de Souza, F.S.J., Nasif, S., Low, M.J., and Rubinstein, M. (2019). The Homeodomain Transcription Factor NKX2.1 Is Essential for the Early Specification of Melanocortin Neuron Identity and Activates Pomc Expression in the Developing Hypothalamus.

J. Neurosci. *39*, 4023–4035. https://doi.org/10.1523/JNEUROSCI.2924-18.2019.

51. Salvatierra, J., Lee, D.A., Zibetti, C., Duran-Moreno, M., Yoo, S., Newman, E.A., Wang, H., Bedont, J.L., de Melo, J., Miranda-Angulo, A.L., et al. (2014). The LIM homeodomain factor Lhx2 is required for hypothalamic tanycyte specification and differentiation. J. Neurosci. *34*, 16809–16820. https://doi.org/10.1523/JNEUROSCI.1711-14.2014.
52. Xu, Q., Tam, M., and Anderson, S.A. (2008). Fate mapping Nkx2.1-lineage cells in the mouse telencephalon. J. Comp. Neurol. *506*, 16–29. https://doi.org/10.1002/cne.21529.
53. Campbell, J.N., Macosko, E.Z., Fenselau, H., Pers, T.H., Lyubetskaya, A., Tenen, D., Goldman, M., Verstegen, A.M.J., Resch, J.M., McCarroll, S.A., et al. (2017). A molecular census of arcuate hypothalamus and median eminence cell types. Nat. Neurosci. *20*, 484–496. https://doi.org/10.1038/nn.4495.
54. Chen, R., Wu, X., Jiang, L., and Zhang, Y. (2017). Single-Cell RNA-Seq Reveals Hypothalamic Cell Diversity. Cell Rep. *18*, 3227–3241. https://doi.org/10.1016/j.celrep.2017.03.004.
55. Campbell, R.E., ffrench-Mullen, J.M., Cowley, M.A., Smith, M.S., and Grove, K.L. (2001). Hypothalamic circuitry of neuropeptide Y regulation of neuroendocrine function and food intake via the Y5 receptor subtype. Neuroendocrinology *74*, 106–119. https://doi.org/10.1159/000054676.
56. Krashes, M.J., Koda, S., Ye, C., Rogan, S.C., Adams, A.C., Cusher, D.S., Maratos-Flier, E., Roth, B.L., and Lowell, B.B. (2011). Rapid, reversible activation of AgRP neurons drives feeding behavior in mice. J. Clin. Invest. *121*, 1424–1428. https://doi.org/10.1172/JCI46229.
57. Lee, B., Kim, J., An, T., Kim, S., Patel, E.M., Raber, J., Lee, S.K., Lee, S., and Lee, J.W. (2018). Dlx1/2 and Otp coordinate the production of hypothalamic GHRH- and AgRP-neurons. Nat. Commun. *9*, 2026. https://doi.org/10.1038/s41467-018-04377-4.
58. Yee, C.L., Wang, Y., Anderson, S., Ekker, M., and Rubenstein, J.L.R. (2009). Arcuate nucleus expression of NKX2.1 and DLX and lineages expressing these transcription factors in neuropeptide Y(+), proopiomelanocortin(+), and tyrosine hydroxylase(+) neurons in neonatal and adult mice. J. Comp. Neurol. *517*, 37–50. https://doi.org/10.1002/cne.22132.
59. Yan, H., Zhang, L., Cui, X., Zheng, S., and Li, R. (2022). Roles and mechanisms of the m6A reader YTHDC1 in biological processes and diseases. Cell Death Discov. *8*, 237. https://doi.org/10.1038/s41420-022-01040-2.
60. Zhang, F., Yoon, K., Kim, N.S., Ming, G.L., and Song, H. (2023). Cell-autonomous and non-cell-autonomous roles of NKCC1 in regulating neural stem cell quiescence in the hippocampal dentate gyrus. Stem Cell Rep. *18*, 1468–1481. https://doi.org/10.1016/j.stemcr.2023.05.021.
61. Berg, D.A., Su, Y., Jimenez-Cyrus, D., Patel, A., Huang, N., Morizet, D., Lee, S., Shah, R., Ringeling, F.R., Jain, R., et al. (2019). A Common Embryonic Origin of Stem Cells Drives Developmental and Adult Neurogenesis. Cell *177*, 654–668.e15. https://doi.org/10.1016/j.cell.2019.02.010.
62. Oliva, C.A., Montecinos-Oliva, C., and Inestrosa, N.C. (2018). Wnt Signaling in the Central Nervous System: New Insights in Health and Disease. Prog. Mol. Biol. Transl. Sci. *153*, 81–130. https://doi.org/10.1016/bs.pmbts.2017.11.018.
63. Liu, P., Li, F., Lin, J., Fukumoto, T., Nacarelli, T., Hao, X., Kossenkov, A.V., Simon, M.C., and Zhang, R. (2021). m6A-independent genome-wide METTL3 and METTL14 redistribution drives the senescence-associated secretory phenotype. Nat. Cell Biol. *23*, 355–365. https://doi.org/10.1038/s41556-021-00656-3.
64. Li, M., Zhao, X., Wang, W., Shi, H., Pan, Q., Lu, Z., Perez, S.P., Suganthan, R., He, C., Bjørås, M., and Klungland, A. (2018). Ythdf2-mediated m6A mRNA clearance modulates neural development in mice. Genome Biol. *19*, 69. https://doi.org/10.1186/s13059-018-1436-y.
65. Huang, W.K., Wong, S.Z.H., Pather, S.R., Nguyen, P.T.T., Zhang, F., Zhang, D.Y., Zhang, Z., Lu, L., Fang, W., Chen, L., et al. (2021). Generation of hypothalamic arcuate organoids from human induced pluripotent stem cells. Cell Stem Cell *28*, 1657–1670.e10. https://doi.org/10.1016/j.stem.2021.04.006.
66. Gao, X., Shin, Y.H., Li, M., Wang, F., Tong, Q., and Zhang, P. (2010). The fat mass and obesity associated gene FTO functions in the brain to regulate postnatal growth in mice. PLoS One *5*, e14005. https://doi.org/10.1371/journal.pone.0014005.
67. Cepko, C. (2014). Intrinsically different retinal progenitor cells produce specific types of progeny. Nat. Rev. Neurosci. *15*, 615–627. https://doi.org/10.1038/nrn3767.
68. Kohwi, M., and Doe, C.Q. (2013). Temporal fate specification and neural progenitor competence during development. Nat. Rev. Neurosci. *14*, 823–838.
69. Wen, Z., Nguyen, H.N., Guo, Z., Lalli, M.A., Wang, X., Su, Y., Kim, N.S., Yoon, K.J., Shin, J., Zhang, C., et al. (2014). Synaptic dysregulation in a human iPS cell model of mental disorders. Nature *515*, 414–418. https://doi.org/10.1038/nature13716.
70. Macosko, E.Z., Basu, A., Satija, R., Nemesh, J., Shekhar, K., Goldman, M., Tirosh, I., Bialas, A.R., Kamitaki, N., Martersteck, E.M., et al. (2015). Highly Parallel Genome-wide Expression Profiling of Individual Cells Using Nanoliter Droplets. Cell *161*, 1202–1214. https://doi.org/10.1016/j.cell.2015.05.002.
71. Yu, G., Wang, L.G., and He, Q.Y. (2015). ChIPseeker: an R/Bioconductor package for ChIP peak annotation, comparison and visualization. Bioinformatics *31*, 2382–2383. https://doi.org/10.1093/bioinformatics/btv145.
72. Love, M.I., Huber, W., and Anders, S. (2014). Moderated estimation of fold change and dispersion for RNA-seq data with DESeq2. Genome Biol. *15*, 550. https://doi.org/10.1186/s13059-014-0550-8.
73. Saunders, A., Macosko, E.Z., Wysoker, A., Goldman, M., Krienen, F.M., de Rivera, H., Bien, E., Baum, M., Bortolin, L., Wang, S., et al. (2018). Molecular Diversity and Specializations among the Cells of the Adult Mouse Brain. Cell *174*, 1015–1030.e16. https://doi.org/10.1016/j.cell.2018.07.028.
74. Cui, X., Wei, Z., Zhang, L., Liu, H., Sun, L., Zhang, S.W., Huang, Y., and Meng, J. (2016). Guitar: An R/Bioconductor Package for Gene Annotation Guided Transcriptomic Analysis of RNA-Related Genomic Features. BioMed Res. Int. *2016*, 8367534. https://doi.org/10.1155/2016/8367534.
75. Heinz, S., Benner, C., Spann, N., Bertolino, E., Lin, Y.C., Laslo, P., Cheng, J.X., Murre, C., Singh, H., and Glass, C.K. (2010). Simple combinations of lineage-determining transcription factors prime cis-regulatory elements required for macrophage and B cell identities. Mol. Cell *38*, 576–589. https://doi.org/10.1016/j.molcel.2010.05.004.
76. Stuart, T., Butler, A., Hoffman, P., Hafemeister, C., Papalexi, E., Mauck, W.M., 3rd, Hao, Y., Stoeckius, M., Smibert, P., and Satija, R. (2019). Comprehensive Integration of Single-Cell Data. Cell *177*, 1888–1902.e21. https://doi.org/10.1016/j.cell.2019.05.031.
77. Dobin, A., Davis, C.A., Schlesinger, F., Drenkow, J., Zaleski, C., Jha, S., Batut, P., Chaisson, M., and Gingeras, T.R. (2013). STAR: ultrafast universal RNA-seq aligner. Bioinformatics *29*, 15–21. https://doi.org/10.1093/bioinformatics/bts635.
78. Bolger, A.M., Lohse, M., and Usadel, B. (2014). Trimmomatic: a flexible trimmer for Illumina sequence data. Bioinformatics *30*, 2114–2120. https://doi.org/10.1093/bioinformatics/btu170.
79. Chiang, C.H., Su, Y., Wen, Z., Yoritomo, N., Ross, C.A., Margolis, R.L., Song, H., and Ming, G.L. (2011). Integration-free induced pluripotent stem cells derived from schizophrenia patients with a DISC1 mutation. Mol. Psychiatry *16*, 358–360. https://doi.org/10.1038/mp.2011.13.
80. Qian, X., Nguyen, H.N., Song, M.M., Hadiono, C., Ogden, S.C., Hammack, C., Yao, B., Hamersky, G.R., Jacob, F., Zhong, C., et al. (2016). Brain-Region-Specific Organoids Using Mini-bioreactors for Modeling ZIKV Exposure. Cell *165*, 1238–1254. https://doi.org/10.1016/j.cell.2016.04.032.

81. Qian, X., Su, Y., Adam, C.D., Deutschmann, A.U., Pather, S.R., Goldberg, E.M., Su, K., Li, S., Lu, L., Jacob, F., et al. (2020). Sliced Human Cortical Organoids for Modeling Distinct Cortical Layer Formation. Cell Stem Cell *26*, 766–781.e9. https://doi.org/10.1016/j.stem.2020.02.002.

82. Jacob, F., Pather, S.R., Huang, W.K., Zhang, F., Wong, S.Z.H., Zhou, H., Cubitt, B., Fan, W., Chen, C.Z., Xu, M., et al. (2020). Human Pluripotent Stem Cell-Derived Neural Cells and Brain Organoids Reveal SARS-CoV-2 Neurotropism Predominates in Choroid Plexus Epithelium. Cell Stem Cell *27*, 937–950.e9. https://doi.org/10.1016/j.stem.2020.09.016.

83. Jacob, F., Salinas, R.D., Zhang, D.Y., Nguyen, P.T.T., Schnoll, J.G., Wong, S.Z.H., Thokala, R., Sheikh, S., Saxena, D., Prokop, S., et al. (2020). A Patient-Derived Glioblastoma Organoid Model and Biobank Recapitulates Inter- and Intra-tumoral Heterogeneity. Cell *180*, 188–204.e22. https://doi.org/10.1016/j.cell.2019.11.036.

84. Hughes, T.K., Wadsworth, M.H., 2nd, Gierahn, T.M., Do, T., Weiss, D., Andrade, P.R., Ma, F., de Andrade Silva, B.J., Shao, S., Tsoi, L.C., et al. (2020). Second-Strand Synthesis-Based Massively Parallel scRNA-Seq Reveals Cellular States and Molecular Features of Human Inflammatory Skin Pathologies. Immunity *53*, 878–894.e7. https://doi.org/10.1016/j.immuni.2020.09.015.

85. Hao, Y., Hao, S., Andersen-Nissen, E., Mauck, W.M., 3rd, Zheng, S., Butler, A., Lee, M.J., Wilk, A.J., Darby, C., Zager, M., et al. (2021). Integrated analysis of multimodal single-cell data. Cell *184*, 3573–3587.e29. https://doi.org/10.1016/j.cell.2021.04.048.

86. Schwartz, S., Agarwala, S.D., Mumbach, M.R., Jovanovic, M., Mertins, P., Shishkin, A., Tabach, Y., Mikkelsen, T.S., Satija, R., Ruvkun, G., et al. (2013). High-resolution mapping reveals a conserved, widespread, dynamic mRNA methylation program in yeast meiosis. Cell *155*, 1409–1421. https://doi.org/10.1016/j.cell.2013.10.047.

87. da Huang, W., Sherman, B.T., and Lempicki, R.A. (2009). Systematic and integrative analysis of large gene lists using DAVID bioinformatics resources. Nat. Protoc. *4*, 44–57. https://doi.org/10.1038/nprot.2008.211.

STAR★METHODS

KEY RESOURCES TABLE

REAGENT or RESOURCE	SOURCE	IDENTIFIER
Antibodies		
Guinea Pig anti-Rx	Clontech	Cat#: M229; RRID: AB_2783559
Goat anti-TBX3	Novus Biologicals	Cat#: AF-4509; RRID: AB_2240328
Goat anti-TBX3	Santa Cruz	Cat#: sc-17181; RRID: AB_661666
Mouse anti-NeuN	Thermo Fisher Scientific	Cat#: MA5-33103; RRID: AB_2802653
Rat anti-BrdU	Abcam	Cat#: ab6326; RRID: AB_305426
Rabbit anti-β-Actin	Cell Signaling Technology	Cat#: 4967; RRID: AB_330288
Rabbit anti-IgG	Cell Signaling Technology	Cat#: 2729; RRID: AB_1031062
Rabbit anti-m6A(kit)	New England Biolabs	Cat#: E1610S
Rabbit anti-m6A	Synaptic Systems	Cat#: 202 003; RRID: AB_2279214
Rabbit anti-METTL14	Sigma-Aldrich	Cat#: HPA038002; RRID: AB_10672401
Rabbit anti-TTF1(NKX2.1)	Abcam	Cat#: ab76013; RRID: AB_1310784
Rabbit anti-OTP	ABclonal	Cat#: A13188; RRID: AB_2760039
Rabbit anti-POMC	Phoenix Pharmaceuticals	Cat#: H-029-30; RRID: AB_2307442
Rabbit anti-TH	Novus Biologicals	Cat#: NB300-109; RRID: AB_350437
Sheep anti-a-MSH	Abcam	Cat#:AB5087; RRID:AB_91683
Chemicals, peptides, and recombinant proteins		
20% Ficoll solution	Sigma-Aldrich	Cat#: F5415
10x RIPA Buffer	Abcam	Cat#: ab156034
10x Tris/Glycine/SDS	Bio-Rad	Cat#: 1610772
4x Laemmli Sample Buffer	Bio-Rad	Cat#: 1610747
A83-01	StemCell Technologies	Cat#: 72022
Actinomycin D	Sigma-Aldrich	Cat#: A1420
AggreWell™800	StemCell Technologies	Cat#: 34815
AMPure XP	Beckman Coulter	Cat#: A63881
Anti-Adherence Rinsing Solution	StemCell Technologies	Cat#: 07010
B-27 Supplement (50X), minus vitamin A	Thermo Fisher Scientific	Cat#: 12587010
B-27 Supplement (50X)	Thermo Fisher Scientific	Cat#: 17504044
Barcoded Beads	ChemGenes	Cat#: MACOSKO-2011-10 B
Blue Protein Loading Dye	New England Biolabs	Cat#:B7703S
BrdU	Sigma-Aldrich	Cat#: B9285
BSA	Sigma-Aldrich	Cat#: A8412
Buffer RLT	Qiagen	Cat#: 79216
Chloroform	Sigma-Aldrich	Cat#: 2432
DAPI	Thermo Fisher Scientific	Cat#: D1306; RRID: AB_2629482
D-(+)Glucose	Sigma-Aldrich	Cat#: G8270
DirectPCR Lysis Reagent	Fisher Scientific	Cat#: 101T
Dimethyl sulfoxide (DMSO)	New England Biolabs	Cat#: 12611
Dulbecco's Modification of Eagle's Medium (DMEM)	Corning	Cat#:10-013
Dulbecco's Modified Eagle Medium/Nutrient Mixture F-12 (DMEM/F-12)	Thermo Fisher Scientific	Cat#: 11320033
dNTP	Takara	Cat#: 639132
Donkey serum	Millipore	Cat#: S30-100ML

(*Continued on next page*)

Continued

REAGENT or RESOURCE	SOURCE	IDENTIFIER
DPBS	Thermo Fisher Scientific	Cat#: 14040133
DTT	Sigma-Aldrich	Cat#: 43816
Dynabeads MyOne Silane	Thermo Fisher Scientific	Cat#: 37002D
EDTA-free Protease Inhibitor Cocktail	Sigma-Aldrich	Cat#:4693159001
EDTA, pH 8.0	Invitrogen	Cat#: 15575020
Exo I	New England Biolabs	Cat#: M0293S
Fetal Bovine Serum (FBS)	Corning	Cat#:35-010
Formaldehyde, 16%, Methanol Free, Ultra Pure	Polysciences	Cat#18814-10
Foskolin	Sigma-Aldrich	Cat#: 344270
Glutamine	GIBCO	Cat#:A2916801
GlutaMAX Supplement	GIBCO	Cat#: 35050061
Hibernate-A medium	Thermo Fisher Scientific	Cat#: A1247501
Human insulin solution	Sigma-Aldrich	Cat#: I9278
IGEPAL CA-630	Sigma-Aldrich	Cat#: I8896
LDN-193189	StemCell Technologies	Cat#: 72147
LipoD293 In Vitro DNA Transfection Reagent	SignaGen Lab	Cat#: SL100668
Klenow Fragment (3'→5' exo-)	Fisher scientific	Cat#: 50305912
KnockOut Serum Replacement	Thermo Fisher Scientific	Cat#:10828028
mTeSR Plus	StemCell Technologies	Cat#: 5825
Matrigel hESC-Qualified Matrix	Corning	Cat#:354234
Maxima H Minus Reverse Transcriptase	Invitrogen	Cat#: EP0752
NaCl	Thermo Fisher Scientific	Cat#: AM9760G
Neurobasal medium	Thermo Fisher Scientific	Cat#: 21103049
NxGen RNase Inhibitor	Lucigen	Cat#: 30281-1
N-Lauroylsarcosine sodium salt solution	Sigma-Aldrich	Cat#: L7414
N-2 Supplement	GIBCO	Cat#: 17502048
Paraformaldehyde Granular	Electron Microscopy Sciences	Cat#: 19210
Pierce™ 16% Formaldehyde	Thermo Fisher Scientific	Cat#: 28906
Penicillin-Streptomycin	Thermo Fisher Scientific	Cat#: 15070063
Perfluorooctanol (PFO)	Sigma-Aldrich	Cat#: 370533
Polyethylene glycol (PEG) solution, 40%	Sigma-Aldrich	Cat#: P1458
Poly-D-Lysine solution	Sigma-Aldrich	Cat#:A-003-E
Protein G Magnetic Beads	New England Biolabs	Cat#: S1430S
Proteinase K	Qiagen	Cat#: 19131
QX200™ Droplet Generation Oil	Bio-Rad	Cat#: 1864006
Recombinant Human BDNF	Peprotech	Cat#: 45002
Recombinant Human CNTF	R&D systems	Cat#: 257-NT
Recombinant Human EGF	Peprotech	Cat#: AF-100-15
Recombinant Human FGF	Peprotech	Cat#: AF-100-18B
Retinoic acid	Sigma-Aldrich	Cat#: R2625
RNA Fragmentation Reagents	Thermo Fisher Scientific	Cat#: AM8740
SB-431542	StemCell Technologies	Cat#:72234
SPRIselect	Beckman Coulter	Cat#: B23317
SSC Buffer	Sigma-Aldrich	Cat#: SRE0068
StemPro Accutase Cell Dissociation Reagent	Thermo Fisher Scientific	Cat#: A1110501
Sucrose	Sigma-Aldrich	Cat#: S5016
SuperSignal West Dura Extended Duration Substrate	Thermo Fisher Scientific	Cat#: 37071
Target Retrieval Solution	Agilent	Cat#: S169984-2

(*Continued on next page*)

Continued

REAGENT or RESOURCE	SOURCE	IDENTIFIER
Thermo Scientific Shandon Immu-Mount	Fisher scientific	Cat#: 9990402
Tissue freezing medium	GeneralData	Cat#:15-183-13
Titanium DNA Polymerase	Takara	Cat#: 639209
Tris HCl, pH 7.0	Invitrogen	Cat#: AM9850G
Tris HCl, pH 7.4	Fisher scientific	Cat#: BMA51237
Tris HCl, pH 8.0	Invitrogen	Cat#: 15568
Triton X-100	Sigma-Aldrich	Cat#: T9284
TRIzol Reagent	Thermo Fisher Scientific	Cat#: 10296028
Trypan blue stain	Thermo Fisher Scientific	Cat#: T10282
TWEEN 20	Sigma-Aldrich	Cat#: P1379
Y-27632	Cellagen Technology	Cat#: C9127-2s
Critical commercial assays		
Rabbit anti-m6A(kit)	New England Biolabs	Cat#: E1610S
Dynabeads™ mRNA DIRECT™ Purification Kit	Invitrogen	Cat#: 61011
Fast SYBR™ Green Master Mix	Thermo Fisher Scientific	Cat#: 4385612
KAPA HiFi Hotstart Readymix	Kapa Biosystems	Cat#: KK2602
KAPA Library Quantification Kit for Illumina NGS	Kapa Biosystems	Cat#: KK4835
Monarch RNA Cleanup Kit	New England Biolabs	Cat#: T2030
NEBNext Ultra II RNA Library Prep Kit for Illumina	New England Biolabs	Cat#: E7770S
Nextera XT Library Prep Kit	Ilumina	Cat#: FC-131-1024
NextSeq High Output v2 75 Cycles	Ilumina	Cat#: TG-160-2005
Papain Dissociation System	Worthington	Cat#: LK003150
Pierce Rapid Gold BCA Protein Assay Kit	Thermo Fisher Scientific	Cat#: A53226
Qubit dsDNA HS Assay Kit	Thermo Fisher Scientific	Cat#: Q32851
RNA Clean & Concentrator-5	Zymo Research	Cat#: R1015
SuperScript™ IV Reverse Transcriptase	Thermo Fisher Scientific	Cat#: 18090050
Ultra sensitive mouse insulin ELISA kit	Crystal Chem	Cat#: 90080
Deposited data		
Mouse single-cell RNA sequencing	This Paper	GEO: GSE26720
Bulk RNA sequencing	This Paper	GEO: GSE267199
m^6A sequencing	This Paper	GEO: GSE267202 and GSE289462
Experimental models: Cell lines		
C12 (iPSC from normal human foreskin fibroblasts)	Wen et al.[69]	N/A
Human: HEK293 Cell Line	ATCC	Cat#CRL-1573
Experimental models: Organisms/strains		
Mouse: Adult C57Bl6/J	Charles River	Cat#: CRL:027; RRID: IMSR_CRL:027
Mouse: Nkx2.1-Cre: C57BL/6J-Tg(Nkx2-1-cre)2Sand/J	Jackson laboratory	Cat#: 008661; RRID: IMSR_JAX:008661
Mouse: Mettl14fl/fl C57Bl6/J	Yoon et al.[20]	N/A
Mouse: Mettl3fl/fl C57Bl6/J	From Dr. Brian C. Capell	N/A
Mouse: Ythdf2fl/fl C57Bl6/J	From Dr. Chuan He	N/A
Mouse: Ythdc1fl/fl C57Bl6/J	From Dr. Jeremy Wang	N/A
Oligonucleotides		
Custom Read 1 Primer: 5'-GCCTGTCCGCGGAAGCAGTGGTATCAACGCAGAGTAC-3'	Macosko et al.[70]	N/A

(*Continued on next page*)

Continued

REAGENT or RESOURCE	SOURCE	IDENTIFIER
P5-TSO hybrid primer: 5'-AATGAT ACGGCGACCACCGAGATCTACA CGCCTGTCCGCGGAAGCAGTGG TATCAACGCAGAGT*A*C-3'	Macosko et al.[70]	N/A
Template Switch Oligo: 5'-AAGCAGTG GTATCAACGCAGAGTACATrGrGrG-3'	Macosko et al.[70]	N/A
TSO-PCR primer: 5'-AAGCAGTGGTA TCAACGCAGAGT-3'	Macosko et al.[70]	N/A
NEBNext Multiplex Oligos for Illumina (Index Primers Set 1)/ 24 reaction	New England Biolabs	Cat#: E7335S
NEBNext Multiplex Oligos for Illumina (Index Primers Set 2)/ 24 reaction	New England Biolabs	Cat#: E7500S
Primers and DNA Oligos Used for qPCR, Cloning and analysis	Table S2	N/A
shRNA sequences	Table S2	N/A
Recombinant DNA		
pCMV-dR8.2 dvpr	Addgene	Cat#: 8455; RRID: Addgene_8455
pCMV-VSV-G	Addgene	Cat#: 8454; RRID: Addgene_8454
pLV-EGFP	Addgene	Cat#: 36083; RRID: Addgene_36083
pLV-EGFP-Cre	Addgene	Cat#: 86805; RRID: Addgene_86805
FUGW	Addgene	Cat#: 14883; RRID: Addgene_14883
Software and algorithms		
Adobe Illustrator CC	Adobe	https://www.adobe.com/products/illustrator.html; RRID: SCR_010279
Bcl2fastq	Illumina	https://support.illumina.com/sequencing/sequencing_software/bcl2fastq-conversion-software.htmlsoftware.html; RRID: SCR_015058
ChIPseeker	Yu et al.[71]	https://onlinelibrary.wiley.com/share/author/GYJGUBYCTRMYJFN2JFZZ?target=10.1002/cpz1.585; RRID:SCR_021322
DAVID	Open source	http://david.abcc.ncifcrf.gov/RRID:SCR_001881
DESeq2 v1.30.1	Love et al.[72]	https://bioconductor.org/packages/release/bioc/html/DESeq2.html; RRID:SCR_015687
Drop-seq tools v.2.5.1	Saunders et al.[73]	https://github.com/broadinstitute/Drop-seq; RRID: SCR_018142
EnhancedVolcano v1.8.0	Github	https://github.com/kevinblighe/EnhancedVolcano; RRID: SCR_018931
Fiji	Open source	http://fiji/sc; RRID: SCR_002285
GraphPad Prism 9	GraphPad Software	http://www.graphpad.com/; RRID: SCR_002798
Guitar	Cui et al.[74]	https://bioconductor.org/packages/Guitar/
HOMER	Heinz et al.[75]	http://homer.ucsd.edu/homer/; RRID:SCR_010881
IGV	Broad Institute	https://www.broadinstitute.org/igv/; RRID: SCR_011793
Morpheus	Broad Institute	http://software.broadinstitute.org/morpheus/; RRID:SCR_014975
R Project v.4.0.3	Open source	https://www.r-project.org/; RRID: SCR_001905
RStudio	Open source	https://rstudio.com/; RRID: SCR_000432
Seurat v4.1.0	Stuart et al.[76]	https://github.com/satijalab/seurat; RRID: SCR_007322
STAR v.2.5.2a	Dobin et al.[77]	http://github.com/alexdobin/STAR; RRID:SCR_015899
Shinycircos	Github	https://github.com/YaoLab-Bioinfo/shinyCircos;

(*Continued on next page*)

Continued		
REAGENT or RESOURCE	SOURCE	IDENTIFIER
Trimmomatic v0.32	Bolger et al.[78]	http://www.usadellab.org/cms/index.php?page=trimmomatic; RRID:SCR_011848
Zen2 Blue	Carl Zeiss	https://www.zeiss.com/microscopy/us/products/microscope-software/zen-lite.html; RRID: SCR_013672
Other		
Bioanalyzer 2100	Agilent	Cat#: G2939BA
4-20% Mini-Gel 15-well, 15 ul	Bio-Rad	Cat#: 4561096
Countess Cell Counting Chamber Slides	Thermo Fisher Scientific	Cat#: C10228
Fuchs-Rosenthal C-Chip	Incyto	Cat#: DHC-F01
One Touch Ultra 2 meter	OneTouch	N/A
OneTouch Ultra Blue Blood Glucose Test Strips	OneTouch	N/A
RNaseZAP	Sigma-Aldrich	Cat#: R2020
Tissue-Tek Cryo Mold Biopsy	Electron Microscopy Sciences	Cat#: 4565
Trans-Blot Turbo Mini 0.2 μm PVDF Transfer Packs	Bio-Rad	Cat#: 1704156

EXPERIMENTAL MODEL AND STUDY PARTICIPANT DETAILS

Animals

All animal procedures used in this study were performed in accordance with the protocol approved by the Institutional Animal Care and Use Committee of the University of Pennsylvania. Animals were housed in temperature and humidity-controlled facilities under 12-hour light/12-hour dark cycle at a constant temperature (23 °C) and with food and water ad libitum. All transgenic mice used in this study were maintained on the C57BL/6 background. The source and information of all genetically modified mice are listed in the key resources table. M14NKO mice were generated by crossing Nkx2.1-Cre$^{Tg/+}$::Mettl14$^{f/f}$ males and Nkx2.1-Cre$^{+/+}$::Mettl14$^{f/f}$ females. M3NKO mice were generated by crossing Nkx2.1-Cre$^{Tg/+}$::Mettl3$^{f/+}$ males and Nkx2.1-Cre$^{+/+}$:: Mettl3$^{f/f}$ females. DF2NKO mice were generated by crossing Nkx2.1-Cre$^{Tg/+}$::Ythdf2$^{f/+}$ males and Nkx2.1-Cre$^{Tg/+}$::Ythdf2$^{f/f}$ females. DC1NKO mice were generated by crossing Nkx2.1-CreTg/+:: Ythdc1f/+ males and Nkx2.1-CreTg/+::Ythdc1f/f females. Mice were genotyped by PCR (Table S2). The time of pregnancy was determined by the presence of a vaginal plug (E0.5). The day of birth was designated as postnatal day 0 (P0).

Primary Mouse Hypothalamic NPC Culture

Mouse NPCs were isolated from E14.5 Mettl14$^{f/f}$ mouse embryonic hypothalamus using papain solution and cultured in DMEM/F12 containing 20 ng/ml FGF2, 20 ng/ml EGF, 2% B27 without VitA, Glutamax, N2 and Penicillin/Streptomycin on culture dishes pre-coated with Matrigel matrix (2%).

Human Induced Pluripotent Stem Cells Culture

The human iPSC line (C1-2) used in the current study was previously generated from male neonatal foreskin fibroblasts from ATCC and has been fully characterized.[69,79–82] Generation of iPSC lines followed institutional IRB and ISCRO guidelines and was approved by Johns Hopkins University School of Medicine. All studies involving human iPSCs were performed in accordance with approved protocols of the University of Pennsylvania. Human iPSCs were cultured on the hESC-qualified Matrigel-coated plates without a feeder and maintained in mTeSR feeder-free maintenance medium. Culture medium was replaced every day. For passaging every 5-7 days, iPSCs were incubated with ReLeSR reagent for 5 mins, and detached iPSC colonies were broken into smaller clusters by trituration with a P1000 pipette.

METHOD DETAILS

Body Weight, Food Intake and Body Metabolic Analysis

The male and female control and M14NKO and DC1NKO mice were fed a chow diet. Body weight was measured weekly. For daily food intake assays, food pellets were weighed at 16:00 each day for one week and an average of four continuous days of food intake was calculated. Mice were subjected to magnetic resonance imaging (MRI) (Echo Medical Systems) to examine body composition. For measurements of energy expenditure, oxygen consumption, CO_2 production and locomoter activity, mice were housed individually in a Comprehensive Lab Animal Monitoring System (CLAMS) (Columbus Instruments) under 12-hour light/12-hour dark conditions for 5 consecutive days. Experimental data were obtained for 3 light/dark cycles after 2 days of an adaptation period.

Glucose and Insulin Test

For glucose tolerance tests, 10 week-old female or 11 week-old male M14NKO mice and their control littermates were fasted for 15 hours and injected with glucose intraperitoneally (1.5 g/kg body weight). Similarly, 20 week-old female DC1NKO mice and their control littermates were fasted for 15 hours and injected with glucose intraperitoneally (1 g/kg body weight). Blood samples were collected at 0, 15, 30, 60, and 120 mins. For insulin tolerance tests, 12 week-old female or 13 week-old male M14NKO mice and their control littermates were fasted for 5 hours and injected with insulin (0.8 U/kg body weight). Similarly, 21 week-old female DC1NKO mice and their control littermates were fasted for 5 hours and injected with insulin (0.8 U/kg body weight). Blood samples were collected at 0, 15, 30, 60, 90, and 120 mins. Glucose levels were measured using test strips. Serum insulin was measured by ELISA after a 15-hour fasting.

H&E Staining

The collected fat tissues were immediately fixed in 10% formalin solution for 48 hours at 4°C and washed with 70% ethanol.[83] Paraffin-embedded tissues were stained with H&E, and images were acquired using Olympus BX43 microscope.

Tissue Microdissection and Dissociation

For micro-dissected hypothalamic arcuate-median eminence complex (ARC–ME) samples, 4 pairs of postnatal day 0 CTRL and NKO mice were dissected, then brains were rapidly extracted and cooled in ice-cold Hibernate-A medium. To obtain coronal sections containing the ARC–ME region, each brain was immersed in melted 3% low melting point agarose dissolved in DMEM kept at 37°C in a custom cryo mold. The agarose mold was placed on ice for 5-10 mins to solidify. Slicing was performed using a Leica VT 1200S vibratome in ice-cold DMEM:F12 medium at 0.1 mm/s speed and 1 mm vibration amplitude. The 250 μm-thick brain slices were separated from the agarose by gentle pipetting and the six consecutive slices from around Bregma -0.96 to – 2.80 mm were collected. The ARC–ME was micro-dissected by knife cuts at its visually approximated dorsolateral borders and pooled for each mouse. Pooled ARC–ME samples were digested by papain solution for 30 mins at 37 °C with gentle agitation. After washing with 5 ml Hibernate A medium, the tissues were triturated with fire-polished glass Pasteur pipettes into a single-cell suspension within Hibernate A medium. To remove debris, the single-cell suspension was loaded on a 2-layer gradient and centrifuged at 100 g for 6 mins at 4oC, and cells were filtered through a 70-μm cell strainer DPBS with 0.01% BSA (w/v). A 10 μl cell suspension was stained with Trypan Blue and the live cells were counted using an automated cell counter (Invitrogen) and manually.

Single-cell RNA-Seq Library Preparation and Sequencing

Samples had a viability of > 80% and were diluted to a final concentration of 100 viable cells/μL in DPBS with 0.01% BSA (w/v). Single cells and barcoded beads were captured into nanoliter-sized droplets and library preparation was performed using the drop-seq method with minor modifications.[70] Each sample was loaded onto 2-3 droplet generation runs, and cell suspensions and droplets were kept on ice prior to droplet encapsulation and droplet breakage. After exonuclease I treatment, second strand synthesis was performed as previously described.[84] In the cDNA PCR amplification stage, around 4,000 beads were combined in a single PCR tube reaction and purified individually using 0.6x AMPure XP beads. cDNA across multiple runs of the same sample were pooled together and used as input for tagmentation, where the tagment reaction time was increased to 6 mins. Final samples were purified twice with 0.6x AMPure XP beads. Sequencing library fragment sizes were quantified by bioanalyzer, and concentrations were quantified by qPCR (KAPA). Samples were pooled, loaded at 2.0-2.2 pM, and sequenced on a Next-Seq 550 (Illumina) with a 20 bp Read 1 and 64 bp Read 2. The custom Read 1 primer was spiked into the usual Illumina sequencing primer well at the manufacturer's recommended concentration.

Single-cell RNA-seq Data Analysis

Raw sequencing data were demultiplexed with bcl2fastq2 with adaptor trimming turned off. Additional processing was performed using drop-seq tools v.2.5.1[73] with GRCm39 as the reference genome. Seurat v4.1.0 was used to analyze most single-cell data.[85] Single cells with > 500 unique genes detected and < 5% mitochondrial counts were retained for further analysis. PCA and UMAP dimensionality reduction were performed using the first 30 empirically selected PCs with standard pipelines. ARC from individual WT mice and M3NKO mice were integrated remove batch effects using the standard scRNA-seq integration workflow in Seurat prior to clustering analysis. We performed clustering as in previous studies[26,33,53,54] and cluster markers were identified using the FindAllMarkers function in Seurat. The cell numbers of each cluster in individual mice were found from Seurat Metadata. The comparison of neuronal clusters between control and M14NKO mice was quantified as a percentage of the total neuron population. The differential gene expression from each cluster was performed by FindMarkers function in Seurat. Volcano plots for differential gene expression were plotted using EnhancedVolcano v1.7.8.

Generation and Differentiation of Mettl14 Knockout Hypothalamic NPCs

We obtained lentiviral vectors expressing either an EGFP-Cre fusion protein or a control EGFP protein from Addgene. For lentivirus production, HEK293T cells were cultured under standard conditions in DMEM supplemented with 10% fetal bovine serum and Penicillin/Streptomycin. HEK293T cells were seeded at 1.1×10^7 cells/dish in three 15-cm dishes the day before transfection. Cells were transfected using LipD293 with pCMV-VSV-G, pCMV-dR8.2dvpr and lentiviral vectors. The medium was collected 48 and 72 hours after transfection, centrifuged by 800g for 10 mins. Viral stocks were concentrated by ultracentrifugation in a SW28

Beckman rotor at 100,000 g for 1.5 hours at 4°C. Pellets containing lentivirus were air dried and resuspended at 4°C in 90 μl PBS. For knocking out Mettl14 from mouse hypothalamic NPCs, NPCs were incubated with culture medium containing lenti-EGFP-Cre or lenti-EGFP viruses and the medium was refreshed after a 24-hour incubation period. After 72 hours, we isolated $EGFP^+$ cells using flow cytometry at the Penn Core Facility. To differentiate hypothalamic neurons, we cultured Mettl14 knockout NPCs and control NPCs in neuron basal medium supplemented with 1 μM Forskolin, 1 μM Retinoic Acid, 10 ng/ml BDNF, 10 ng/ml CNTF, 2% B27 with VitA, Glutamax and Penicillin/Streptomycin. Culture dishes were pre-coated with Poly-D-lysine and $EGFP^+$ cells were differentiated for 8 days with media changes every other day.

RNA Isolation and qPCR

Total RNA fraction was isolated from cultured hypothalamic NPCs samples, day 12 human ARCOs and FACS-purified GFP^+ cells from day 40 ARCOs using RNA Clean & Concentration Kit, and reverse-transcribed into first-strand cDNA with SuperScript IV. cDNAs were used for SYBR-green-based quantitative real-time PCR to measure the expression level of target genes. The relative expression level of mRNA was normalized to 36B4. All the primers used for quantitative PCR are listed in Table S2.

RNA-seq, m^6A-seq and Data Analyses

Library preparation was performed as previously described with some minor modifications.[86] Briefly, enrichment of polyadenylated RNA from total RNA was performed using Oligo(dT) dynabeads according to the manufacturer's protocol. The polyadenylated RNA was chemically fragmented into ~80-nt-long fragments using zinc fragmentation reagent. To purify the RNA, 20 μl MyOne Silane Dynabeads were washed in 100 μl RLT, resuspended in 30 μl RLT, and added to the eluted RNA. 60 μl 100% ethanol was added to the mixture, the mixture attached to the magnet and the supernantant discarded. Following two washes in 100 μl of 70% ethanol, the RNA was eluted from the beads in 16.5 μl water. For RNA-seq, 50 ng of polyadenylated RNA fragments from Mettl14 knockout or control NPCs were used for cDNA library preparation with the NEBNext Ultra II RNA Library Prep Kit (NEB, E7770S) following the manufacturer's protocol.

For m6A-seq, enrichment of m^6A modified RNA was obtained using polyadenylated RNA fragments from 30 μg total RNA with the EpiMark N6-Methyladenosine Enrichment Kit (NEB) following the manufacturer's protocol. Then the IP samples were used for cDNA library preparation with the NEBNext Ultra II RNA Library Prep Kit. Sequencing library fragment sizes were quantified by bioanalyzer with an average size of ~400 bp, and concentrations were quantified by qPCR (KAPA). Samples were pooled, loaded at 2.7 pM, and sequenced on a Next-Seq 550 (Illumina).

Raw sequencing data from RNA-seq and m^6A-seq were demultiplexed with bcl2fastq2 v2.17.1.14 (Illumina), and adaptors were trimmed using Trimmomatic v0.32 software with MINLEN.[78] Alignments were made using STAR v2.5.2a[77] to GENCODE mouse reference genome GRCm38.p6 or the GENCODE human reference genome GRCh38.p13. For m^6A-seq analysis, all m^6A modification sites were examined using the BAM file generated from STAR, applying exomePeak2 with criteria of fold change > 2 compared to input and FDR < 0.01). The visualization of all peaks, as well as individual peaks, was obtained using Shinycircos (GitHub) or IGV (Broad Institute). Motif identification analysis was performed using HOMER.[75] The distribution and annotation of peaks were separately conducted using Guitar[74] and ChIPseeker,[71] respectively. For RNA-seq analysis, only uniquely mapped reads were quantified at the gene level and summarized to gene counts using STAR-quantMode (GeneCounts), with multimapping and chimeric alignments discarded. Further analyses were performed in R (v3.6.0). Differential gene expression analysis between control and Mettl14 knockout hypothalamic NPCs was performed using DESeq2[72] (adjust p-value < 0.01 and fold change > 2) and upregulated and downregulated gene lists between control and Mettl14 knockout hypothalamic NPCs were used for Gene Ontology (GO) enrichment analysis using DAVID Bioinformatics Resources.[87] Normalized gene counts of genes calculated by DESeq2 were converted to row Z-scores per gene for visualization in heatmaps using Morpheus (Broad Institute). The shared and unique signatures of upregulated and downregulated genes containing m^6A modifications were visualized using VennDiagram.

Tissue and Organoid Preparation and Sectioning

Mice were transcardially perfused with DPBS followed by 4% paraformaldehyde (PFA). For embryonic samples, timed pregnant females were euthanized by cervical dislocation, and embryos were euthanized by decapitation before dissection. Brains were dissected and post-fixed in 4% PFA for 48 hours at 4°C, and then cryoprotected in 30% sucrose solution overnight at 4°C. All brains were embedded in tissue freezing medium and stored at -80°C before sectioning. Serial coronal brain sections (40 μm for P21 and adult samples, 30 μm for embryonic and P0/P1 samples) were prepared with a cryostat (Leica, CM3050S). ARCOs were first fixed in 4% PFA at room temperature for 1 hour on a tube rotator and dehydrated in 30% sucrose at 4oC overnight. Organoids were embedded in tissue freezing medium and stored at -80°C before sectioning. Organoid sections (25 μm) were sliced with a cryostat.

Immunohistology and Confocal Imaging

Brain sections on slides were washed in TBS and underwent antigen retrieval with Sodium Citrate Buffer. After washing in TBS, brain and organoid sections were blocked and permeabilized with blocking solution (5% normal donkey serum and 0.1% Triton X-100 in TBS) for 1 hour at room temperature. Brain and organoid sections were then incubated with primary antibodies in blocking solution for 24 hours at 4°C. All primary antibodies used in this study are listed in the key resources table. After washing in TBS, brain sections were incubated with secondary antibodies in blocking solution for 2 hours at room temperature. Secondary antibodies (Cy2 or Alexa Fluor 488, Cy3 or Alexa Fluor 555, Cy5 or Alexa Fluor 647, Jackson ImmunoResearch) were used at a dilution of 1:500. Then nuclei

were visualized by incubating for 10 min with DAPI in PBS. Sections were then washed in TBS and mounted with mounting media. Images were acquired with Zeiss LSM 800 confocal microscopes with a 20X, or 40x objective. Images were analyzed using Fiji and Adobe Photoshop software. The brightness and contrast of entire images were adjusted as necessary for visualization. For cell counting, the Tile Scan model was used to cover the target regions. Three Z sections with 1 μm intervals (3 μm thick) were collected with Z stack Acquisition model. The average Intensity Projections of three Z sections were exported as PNG or TIFF format images.

BrdU Birth-Dating Analysis

BrdU (Bromodeoxyuridine) pulse labeling was used to analyze the birth-dating of neurons in the ARC of CTRL and M14NKO mice or CTRL and DC1NKO mice. A stock solution of BrdU (10 mg/ml) was made in saline solution (0.9%). For M14NKO mice, a single injection of BrdU (50 mg/kg, body weight) was administered intraperitoneally to the timed pregnant females (at E12.5 and E15.5). Birth-dating analysis of the ARC neurons was performed at P21. For DC1NKO mice, a single injection of BrdU (50 mg/kg, body weight) was administered intraperitoneally to the timed pregnant females (at E13.5). Birth-dating analysis of the ARC neurons was performed at P1. Brain sections stained for BrdU were incubated in HCl solution for one hour at room temperature and then washed in sodium borate buffer (0.1 M sodium tetraborate decahydrate, pH 8.5). After washing in TBS, brain sections were immunostained with standard protocols. For birth-dating analysis, $BrdU^+NeuN^+$ cells were quantified to analyze the birth-dating of ARC neurons. $BrdU^+POMC^+$ cells were quantified to analyze the birth-dating of $POMC^+$ neurons.

Generation of ARCOs from Feeder-free Human iPSCs

Generation of organoids was performed similar to previous feeder methods with modifications.[65] Human iPSC colonies were detached with ReLeSR reagent for 5 mins, transferred to ultra-low Attachment U-bottom 96-well plates (20K cells/well) and cultured in mTeSR feeder-free maintenance media supplemented with 10 mM Y-27632 (StemcellTech) for 24 hours for Embryoid Body (EB) aggregation. On Day 2, EBs were transferred to an ultra-low attachment 6-well plate (Corning Costar), containing induction medium I consisting of DMEM:F12 supplemented with 20% KnockOut Serum Replacement, 1% MEM-NEAAs, 1% GlutaMAX, 0.1 mM 2-mercaptoethanol, 0.0002% heparin, plus 1 μM LDN, 5 μM SB, 10 μM IWR1-endo, 1 μM SAG, 1 μM purmorphamine, and 50 ng/mL recombinant Sonic Hedgehog. Organoids were placed on a CO_2 resistant orbital shaker (ThermoFisher) starting from Day 2. On Day 6, organoids were transferred to induction medium II (same as the induction medium I but excluding 20% KnockOut Serum Replacement, 0.0002% heparin, 1 μM LDN, and 5 μM SB). From Day 12, organoids were transferred to differentiation medium consisting of 20 ng/ml CNTF, 20 ng/ml BDNF, 20 ng/ml GDNF, 1X B27 Supplement, 0.5 μM Dibutyryl-cAMP, 0.2 mM Ascorbic Acid, 1X GlutaMAX, and 1X NEAA. Organoids were maintained with media changes every other day.

shRNA Lentivirus Production and Infection of Organoids

To construct the shRNA lentivirus, a short hairpin RNA sequence (Table S2) was cloned into the lentiviral vector expressing GFP under the control of the human ubiquitin C promoter and the specific shRNA under the control of human U6 promoter (FUGW) as previously described.[20] The process of packaging and generating lentiviral shRNA has been previously described as above. For knocking down *METTL14* or *YTHDC1* in human hypothalamic NPCs, organoids were incubated with induction medium II containing lentivirus on day 11. To enhance the transduction efficiency of lentiviral vectors, we placed 4 to 5 organoids in a single well of a 96-well plate. Subsequently, 40 μL of medium containing lentivirus (~30 MOI) was added to each well, and the medium was refreshed after a 24-hour incubation period. Organoids were fixed for analysis at day 40.

Protein Extraction and Western Blot

Control and knockout hypothalamic NPCs were lysed in RIPA buffer with protease inhibitor cocktail. Lysates were incubated for 15 mins on ice and centrifuged at 12,000 g for 15 mins at 4°C. The supernatant was collected and boiled for 5 mins in loading buffer (NEB), resolved by 4-20% Mini-Gel, transferred to a PVDF membrane, and immunoblotted. Primary antibodies are listed in the key resources table. Quantification of bands was performed using ImageJ software.

QUANTIFICATION AND STATISTICAL ANALYSIS

The data presented in the figure panels represent multiple independent experiments conducted on separate days. The variation within each data group is indicated using the standard error of the mean (SEM). To assess the significance of differences between two treatments, unpaired Student's t-tests were conducted (refer to each figure for specific details).